Role of strain localization and melt flow on exhumation of deeply subducted continental crust

Prokop Závada[1,2], Karel Schulmann[2,3], Martin Racek[4], Pavlína Hasalová[2], Petr Jeřábek[4], Roberto F. Weinberg[5], Pavla Štípská[2,3], and Alice Roberts[5]

[1]INSTITUTE OF GEOPHYSICS ASCR (ACADEMY OF SCIENCES OF THE CZECH REPUBLIC), V.V.I., BOČNÍ II 1A/1401, PRAGUE 4, 14131, CZECH REPUBLIC
[2]CENTER FOR LITHOSPHERIC RESEARCH, CZECH GEOLOGICAL SURVEY, KLÁROV 3, PRAGUE 1, 11821, CZECH REPUBLIC
[3]UNIVERSITÉ DE STRASBOURG, CNRS (CENTRE NATIONAL DE LA RECHERCHE SCIENTIFIQUE), INSTITUT DE PHYSIQUE DU GLOBE DE STRASBOURG, UMR (UNITÉ MIXTE RECHERCHÉ) 7516, 67084 STRASBOURG, FRANCE
[4]INSTITUTE OF PETROLOGY AND STRUCTURAL GEOLOGY, FACULTY OF SCIENCE, CHARLES UNIVERSITY, ALBERTOV 6, PRAGUE 2, 128 43, CZECH REPUBLIC
[5]SCHOOL OF EARTH, ATMOSPHERE AND THE ENVIRONMENT, MONASH UNIVERSITY, VICTORIA 3800, AUSTRALIA

ABSTRACT

A section of anatectic felsic rocks from a high-pressure (>13 kbar) continental crust (Variscan Bohemian Massif) preserves unique evidence for coupled melt flow and heterogeneous deformation during continental subduction. The section reveals layers of migmatitic granofels interlayered with anatectic banded orthogneiss and other rock types within a single deformation fabric related to the prograde metamorphism. Granofels layers represent high strain zones and have traces of localized porous melt flow that infiltrated the host banded orthogneiss and crystallized granitic melt in the grain interstices. This process is inferred from: (1) gradational contacts between orthogneiss and granofels layers; (2) grain size decrease and crystallographic preferred orientation of major phases, compatible with oriented growth of crystals from interstitial melt during granular flow, accommodated by melt-assisted grain boundary diffusion creep mechanisms; and (3) pressure-temperature equilibria modeling showing that the melts were not generated in situ. We further argue that this porous melt flow, focused along the deformation layering, significantly decreases the strength of the crustal section of the subducting continental lithosphere. As a result, detachment folds develop that decouple the shallower parts of the layered anatectic sequence from the underlying and continuously subducting continental plate, which triggers exhumation of this anatectic sequence.

INTRODUCTION

Weakening of rocks by interstitial melt plays a significant role in the dynamics of orogenic systems (e.g., Vanderhaeghe 2009; Jamieson et al., 2010) and can result in large displacements along melt-bearing shear zones bounding regions of rapid uplift (Hollister and Crawford, 1986), extrusion of lower crustal rocks along orogenic sutures (Konopásek and Schulmann, 2005; Möller et al., 2015), or channel flow of partially molten lower crust during intracrustal indentation (Beaumont et al., 2001; Vanderhaeghe et al., 2003; Culshaw et al., 2006; Jamieson et al., 2007; Schulmann et al., 2008a; Maierová et al., 2012). Labrousse et al. (2015) suggested that melting of subducted upper continental crust at ultrahigh-pressure (UHP) conditions triggers its subsequent exhumation. Labrousse et al. (2015) showed that the partial melting of subducting crust in the subduction channel starts at depths exceeding 100 km, depending on the water content. Increasing amount of buoyant partially molten crust subsequently detaches

from the subducting plate and rises upward in the form of a diapir-like structure. In contrast, based on a different numerical modeling study, Butler et al. (2015) argued that melting in subducted crust has only minor, if any effect on exhumation, at least for large UHP terranes, for example the Western Gneiss Region in Norway. However, numerical model results might be biased by the approach chosen to introduce the melt-enhanced weakening (Jamieson and Beaumont, 2011; Labrousse et al., 2015; Butler et al., 2015; Maierová et al., 2016). Furthermore, low resolution of these models (~1 km grid spacing) does not allow simulation of mesoscale to microscale deformation mechanisms coupled with porous melt flow and melt segregation (see Wallner and Schmeling, 2016).

One way to improve our understanding of melt-enhanced weakening coupled with melt transfer at high-pressure (HP) to UHP conditions, is to directly study such former anatectic regions in the field. Grain-scale to mesoscale melt topology studies mostly focus on anatectic high-temperature–medium-pressure regions

that commonly show protracted episodes of melting (e.g., Sawyer, 2001; Brown and Solar, 1999; Hasalová et al., 2008a, 2008b; Kisters et al., 2009; Bonamici and Duebendorfer, 2010; Sawyer, 2014; Hall and Kisters, 2012, 2016). In contrast, petrostructural studies of migmatitic UHP terranes have aimed to identify the incipient melting reactions close to the UHP conditions (e.g., Gordon et al., 2013; Chen et al., 2013, 2015; Ganzhorn et al., 2014; Zhang et al., 2015; Stepanov et al., 2016), and rather neglected the grain-scale melt topology and deformation mechanisms with respect to the kinematic framework of their host. The mechanisms of coupled grain-scale deformation and melt flow in HP felsic crust are so far rather conceptual and inspired by results from material science (e.g., Fusseis et al., 2009), deformation experiments in mantle rocks (e.g., Kohlstedt and Holtzman, 2009), and granular compaction theory (McKenzie, 1984; Veveakis et al., 2015; Weinberg et al., 2015). It is anticipated that melt transfer in partially molten rocks at high pressures is driven by either the pressure gradients

during grain boundary sliding at grain scale (e.g., Rosenberg and Handy, 2000; Fusseis et al., 2009; Holtzman et al., 2003; Weinberg and Regenauer-Lieb, 2010; Peč et al., 2015), or by compaction and/or decompaction of the matrix in porous viscoelastic matrix. The mesoscale structures coupled with melt transfer were explained either as ductile compaction instabilities, producing axial planar leucosomes (Weinberg et al., 2015), or porous channels (vug waves; Morgan and Holtzman, 2005; porous waves; Connolly and Podladchikov, 2007; Yarushina et al., 2015).

We have focused on the coupled role of melt transfer and rock deformation in the HP (~9-13 kbar) anatectic metagranitoids of the Eger Crystalline Complex (ECC), in western Czech Republic. The ECC represents a continental crust that has been subducted to UHP conditions underneath a continental plate, which is now exposed at the western margin of the Bohemian massif (e.g., Konopásek and Schulmann, 2005; Kotková and Janák, 2015; Haifler and Kotková, 2016). The ECC consists of granulites and orthogneisses that underwent different degrees of migmatization and deformation, resulting in a wide range of rock types, i.e., banded orthogneiss, migmatite, mylonite, and granofels.

In this study we aim to understand the origin of these different textural types and their relationship. We investigate different possibilities and suggest that the granofels represents banded orthogneiss that was transformed by pervasive grain-scale melt migration along the deformation fabric, as described for example in Závada et al. (2007) or Hasalová et al. (2008a). We demonstrate how such reactive porous flow channels gradually transform the banded orthogneiss into homogeneous granofels through a transitional rock where only relict banding is preserved. We propose that the granofels zones represent principal zones of weakness in the subduction channel and that melt infiltrating the deformed orthogneiss can promote significant weakening of the anatectic multilayer. We also investigate the origin of detachment folds in migmatites that develop above the weakened horizons. We then discuss the role of these folds in the mechanical evolution and exhumation of the HP to UHP rocks.

GEOLOGICAL SETTING

The Variscan orogen exposed in the Bohemian massif was recently interpreted in Schulmann et al. (2009, 2014) as a deeply eroded Andean-type subduction-collisional orogenic system. This model invokes subduction of the Saxothuringian plate beneath the upper plate represented by the Teplá-Barrandian and Moldanubian crust (Fig. 1A) and large-scale relamination

of the subducted and buoyant lower plate felsic crust under the mafic lower crust of the upper plate. The subducted felsic crust likely plunged to upper mantle depths, as indicated by diamond- and coesite-bearing felsic gneisses and granulites (Kotková et al., 2011; Haifler and Kotková, 2016; Nasdala and Massonne, 2000; Stöckhert et al.,

2001) associated with peridotites and eclogites (Kotková and Janák, 2015). These rocks extruded together to the shallower crustal levels of the orogeny along the former suture interface.

The high pressure (HP) anatectic rocks, including the diamond-bearing granulites, form the ECC, which crops out along the Ohře
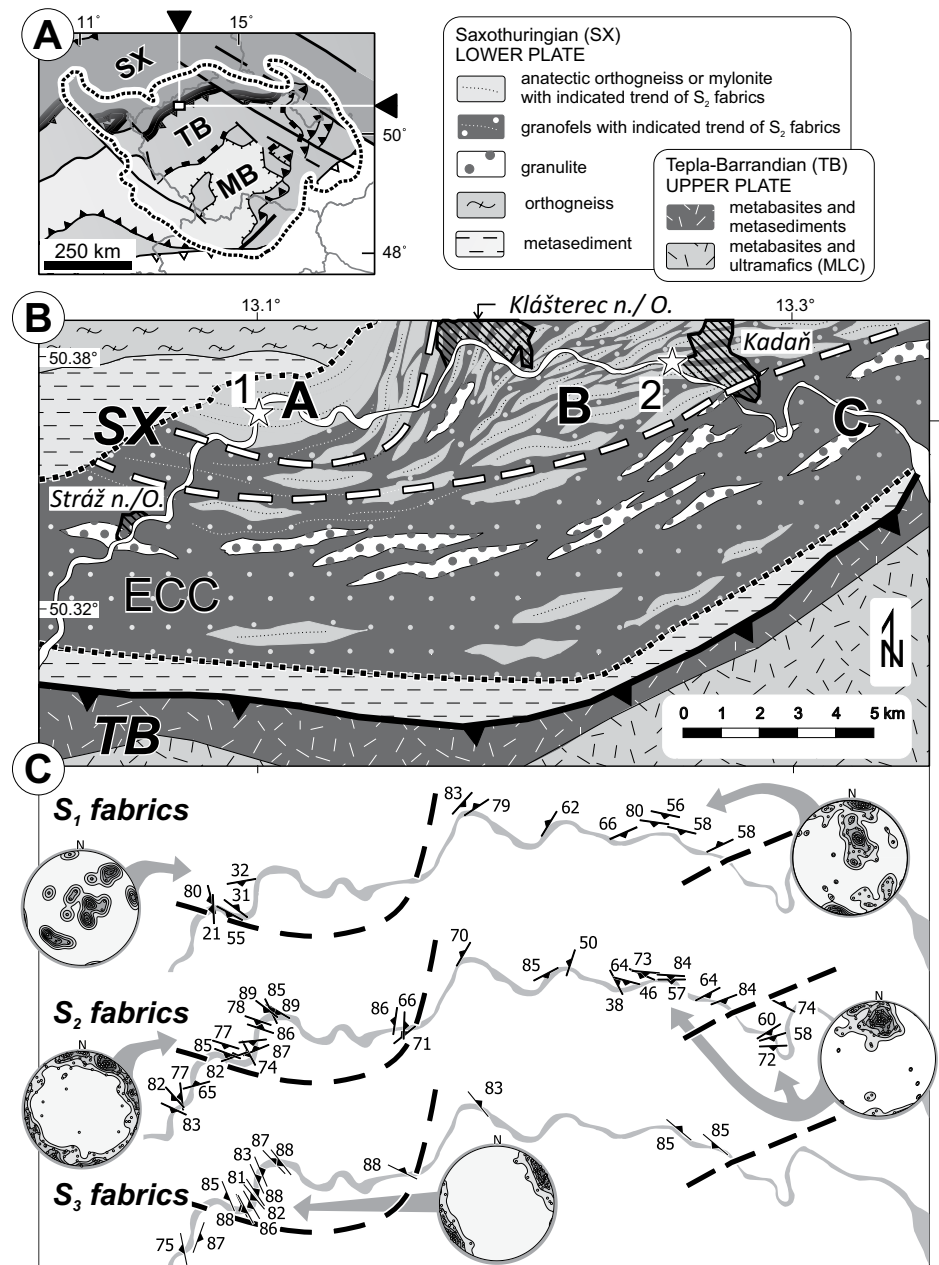
Figure 1. (A) Map of the Eger Crystalline Complex (ECC) with Tertiary cover removed, located at the major Variscan collisional boundary in the Bohemian Massif (BM) shown in the context of the European Variscides. SX—Saxothuringian, TB—Teplá-Barrandian, MB—Moldanubian. (B) The extent of the ECC, outlined with black dotted line, and the contact with the upper plate, was reconstructed on the basis of extensive coal-mining related drillhole surveys (Mlčoch and Konopásek, 2010). Supposed boundaries between respective domains A, B, and C (described in text) are shown by dashed white lines in B and black dashed lines in C. Locations of outcrops shown in Figures 3 and 5 are marked by stars 1 and 2, respectively. Map of the Variscides is simplified after Maierová et al. (2016). (C) Schematic structural maps of the S_1, S_2, and S_3 fabrics in the studied section.

(Eger) river between the towns of Kadaň and Stráž nad Ohří (Fig. 1). The ECC consists of banded orthogneisses, mylonites, migmatites, granofelses, and granulites, as well as of scarce metasedimentary inclusions. Pressure-temperature (P-T) conditions for the banded orthogneiss were estimated at 9 kbar at 700 °C (Závada et al., 2007), while granofels and granulite reveal much higher pressures of ~15 kbar at 760 °C, and 15–16 kbar at 775–840 °C, respectively (Konopásek et al., 2014; Kotková et al., 1996). U-Pb zircon dating revealed protolith ages clustered around ca. 475 Ma for both granofels and granulite (Zulauf et al., 2002; Konopásek et al., 2014), suggesting that they are derived from granitoid protolith of the same age. These ages are similar to other orthogneisses throughout the Saxothuringian domain (e.g., Tichomirowa et al., 2001; Košler et al., 2004). The high-P metamorphism was dated as 342 ± 1 Ma for the banded orthogneiss (U-Pb monazite ages; Zulauf et al., 2002) and as 339 ± 1.5 Ma and 342 ± 10 Ma for the granulites (U-Pb zircon ages; Kotková et al., 1996; Konopásek et al., 2014). Subsequent very fast cooling rates of 50 +25/–17 °C m.y.$^{-1}$ were deduced from ^{40}Ar-^{39}Ar muscovite and biotite cooling ages of 341 ± 4 Ma in the banded orthogneiss (Zulauf et al., 2002). This rapid exhumation is attributed to a significant shift in the orogen dynamics due to the lower slab breakoff and rebound that squeezed the relaminated felsic crust of the lower plate sideways and upward along the margins and the arc region of the orogen (Schulmann et al., 2014). Such fast exhumation rates are necessary for preservation of the peak assemblages in UHP collisional systems (Hollister, 1982; Korchinski et al., 2014).

METHODOLOGY

Selected samples on the outcrops were collected conventionally or cut out from the outcrop using a portable gasoline-powered diamond saw. Extracted slabs were then dimensioned for polished thin sections. To construct the phase and melt topology maps of the entire thin sections, the cathodoluminescence (CL) image mosaics (~90–150 images) were captured using the CITL Mk5–2 CL microscope (http://www.cathodoluminescence.com/) at 700 mA with a capture time of 1.5 s at the Czech Geological Survey in Prague. The images were then stitched together using the software Kolor Autopano GIGA (www.kolor.com). Resulting image mosaics were subjected to image segmentation in ArcMap 10.2.1 (www.esri.com) using the Maximum likelihood classification tool. The results of image segmentation were then transformed to phase maps in the form of shapefiles (Data Repository [DR] File, Figs. DR1, DR2,

DR3[1]) that were then manually corrected and statistically analyzed in MATLAB™ using the PolyLX MATLAB™ toolbox (Lexa et al., 2005). Further details on the image segmentation and analysis procedure are provided in the DR File. In addition, we used an *electron probe microanalyzer* (EPMA) CL device as a complementary tool to study the melt topology alongside the compositional maps (Figs. DR1a, DR3) in the Laboratory of Electron Microscopy and Microanalysis at the Institute of Petrology and Structural Geology (IPSG, Faculty of Science, Charles University, Prague, Czech Republic). An integrated CL spectrometry system xCLent IV was attached to the field-emission gun (FEG) EPMA JXA-8530F (with 15 kV and 40 nA).

The crystallographic preferred orientation (CPO) data of K-feldspar, plagioclase, and quartz in two samples (a mylonite, sample EC12-8G and a granofels, sample EC12-8C2) were acquired using the electron backscattered diffraction (EBSD) in the Laboratory of Electron Microscopy and Microanalysis at the IPSG using the scanning electron microscope Tescan Vega equipped by EBSD detector NordlysNano (manufactured by Oxford Instruments). Automatic mapping of the CPO providing the EBSD maps was acquired at accelerating voltage 20 kV, 39 mm working distance, and ~5 nA beam current and 30 µm step size in automatic mode using the Aztec software (www.aztecsoftware.com/). The CPO data were processed and plotted using the MTEX MATLAB™ toolbox (Hielscher and Schaeben, 2008). To obtain a statistically relevant data set of crystallographic orientations, 11 maps in sample EC12-8G and 7 maps in sample EC12-8C2 were acquired in selected domains that are internally homogeneous (e.g., along the monomineralic layer in the mylonite sample). In addition, three maps (two in sample EC12-8G and one in sample EC12-8C2) of representative domains were acquired at a step size of 7 µm to reliably reconstruct the topology of grain-phase boundaries. The grains reconstructed from EBSD

---

[1]GSA Data Repository Item 2017403, additional information about the methodology and extra datasets associated with the manuscript. The first section in the DR file, "Image analysis of melt topology," explains in detail the image analysis procedure (segmentation) of the cathodoluminescence image mosaics. The second section, "Thermodynamic modeling of PT equilibria," includes the details of phase equilibria modeling for the melt content and pressure and temperature estimations. "Additional datasets" shows additional microstructures in hand line-drawings alongside the cathodoluminescence images, whole-rock and mineral compositional data, and geochemical diagrams comparing the composition of the different anatectic rock types and the leucosomes with respect to the protolith orthogneisses, is available at http://www.geosociety.org/datarepository/2017/, or on request from editing@geosociety.org.

data in MTEX (Bachmann et al., 2011) satisfy a condition of high-angle grain boundaries with 10° misorientation angle between neighboring grains (White and White, 1981). The strength of the preferred orientation, the texture J-index, as defined by Bunge (1982), was calculated in MTEX from the orientation distribution function ODF by Fourier method with de la Vallée Poussin kernel and a half width of 15°. Grain size and axial ratio statistics of the major phases were acquired by manual tracing of the CL images in ArcMap 10.2.1 and statistically processed in PolyLX MATLAB™ toolbox, because a large number of grains in the EBSD maps were truncated on the map boundaries. Alignment of melt pockets was statistically evaluated in rose diagrams as length-weighted manually traced two node line segments.

For chemical analyses of major and trace elements, the samples were crushed with a jaw crusher and pulverized in an agate mill in the laboratories of the Czech Geological Survey in Prague. Pulverized and homogenized samples were analyzed in the Bureau Veritas Mineral Laboratories (Vancouver, Canada). The total whole-rock characterization (code LF202; see http://acmelab.com/pdfs/FeeSchedule-2016.pdf) was done using the lithium borate fusion inductively coupled plasma (ICP)–emission spectrometer (major and minor elements, code LF302) the lithium borate fusion ICP–mass spectrometer (MS) (trace elements, code LF100), and Aqua Regia ICP-ES and ICP-MS (trace elements, code AQ200) methods.

The compositional variation between the selected rock types, evaluated in terms of element transfer in migrating melt, is expressed using the relative abundance of specific element (i) and F_v volume factor in the diagrams of Potdevin (e.g., Potdevin and Marquer, 1987; López-Moro, 2012). While the F_v is given by the volume ratio between the transformed rock and the initial one, the difference in relative abundance of specific element (i) is expressed by:

$$\Delta m_i = F_v \cdot \left(\frac{\rho_a}{\rho_0} \right) C_a^i - C_0^i, \qquad (1)$$

where Δm_i is the relative gain or loss of mass, C_0^i and C_a^i are the initial and final concentrations, and ρ_0 and ρ_a are the densities of these rocks.

The microanalyses of the rock-forming minerals were done at the Laboratory of Electron Microscopy and Microanalysis at the IPSG. They were acquired using the Jeol FEG-EPMA JXA-8530F (accelerating voltage 15 kV, beam current 20 nA). Garnet was analyzed with a focused beam and feldspars and micas were analyzed with a beam defocused to a diameter of 5 µm.

Figure 2. Scans of sections illustrating the range of textures of studied rocks displayed in the Eger Crystalline Complex. All images have the same scale (indicated in D). (A) Banded orthogneiss consists of alternating monomineralic bands of feldspars enclosing the quartz lenses. (B) Mylonitic bands are thinner than those in the orthogneisses. (C) Neosomes surrounding the residual, corroded aggregates of quartz and feldspars (paleosome) in the migmatite are marked by dotted contours and white arrows. (D) Migmatite that consists entirely of the neosome; leucosomes are indicated by black arrows. (E, F, G) Granofelses consist of a homogeneous mixture of primarily feldspars, quartz and white micas. Granofelses in general contain a lower amount of biotite and more muscovite than the orthogneisses (Table 3). (H) Granulite shows fine-grained equigranular texture dominated by felsic minerals.
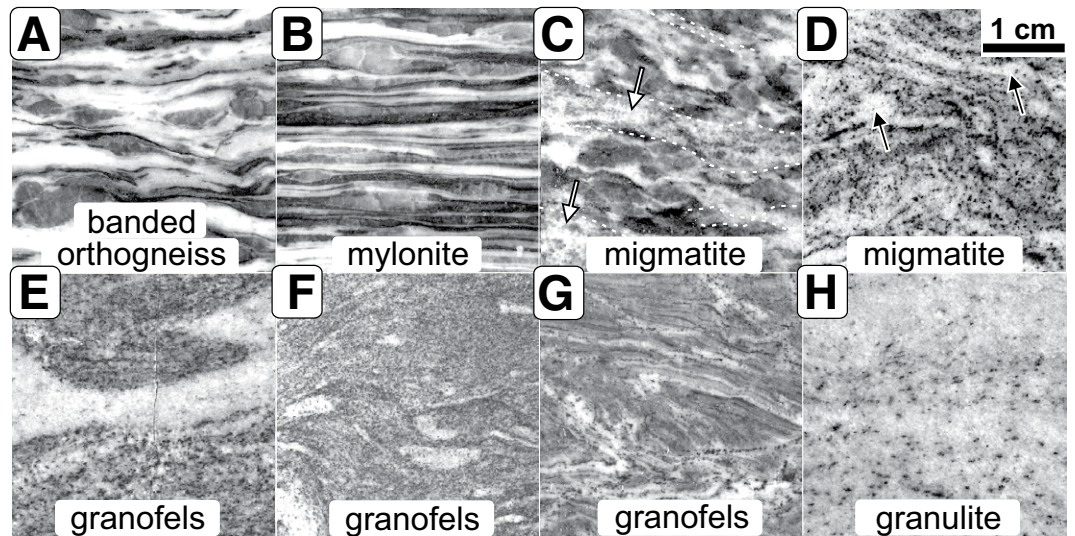
LITHOLOGIES AND DEFORMATION IN THE EGER CRYSTALLINE COMPLEX

We describe here the major types of anatectic rocks studied (Fig. 2), define the terminology used, and recount the succession of deformation fabrics (Fig. 1C). We then describe the structural pattern on the western and eastern part of the studied profile (Figs. 3, 4), and detail the mesoscale features related to anatexis and melt migration on a key outcrop (Figs. 5, 6), that has an excellent record of the earliest fabrics, in the town of Kadaň (Fig. 1B).

Rock Types

Based on the textural appearance and mineral assemblage we have distinguished five main rock types, described here (see Fig. 2). They are ordered in a sequence characterized by the gradual disappearance of monomineralic layering.

Banded orthogneiss is defined as muscovite-biotite-garnet–bearing felsic orthogneiss with alternating ~1-cm-thick feldspar layers and lens-like aggregates of quartz and micas (Fig. 2A).

Mylonite is a highly deformed version of the muscovite-biotite-garnet–bearing banded orthogneiss and is compositionally identical to orthogneisses, but displays thinner bands (Fig. 2B).

Migmatite is defined here as a heterogeneous rock that dominantly consists of two parts; neosome, which represents the newly formed or reconstituted part of the migmatite, and a paleosome, which represents the residual part of the migmatite (Figs. 2C, 2D). Leucosome is the lighter colored part of the neosome, consisting dominantly of quartz and feldspars, and represents crystallized product of the melt. The

migmatites retain their layered structure, can consist entirely of the neosome, and display 5–20 vol% of leucosomes.

Granofels is an isotropic, fine-grained granoblastic metamorphic rock (Figs. 2E–2G) consisting of K-feldspar (10–30 vol%), plagioclase (20–30 vol%), quartz (30–40 vol%), muscovite (10–15 vol%), minor biotite, and garnet (1–5 vol%); it can contain kyanite. Granofels contains leucosomes (5–25 vol%) that form stromata, patches, or networks (Figs. 2E–2G) of leucocratic veins and can resemble patchy or stromatic migmatites (Sawyer, 2008). The color of granofels ranges from dark gray to pinkish white, which reflects the contrasting content of micas and garnet porphyroblasts in the matrix.

Granulite is a felsic granulite (Fig. 2H) that differs from granofels by presence of kyanite and a lack of muscovite and leucosomes. It has typical mineral assemblage of K-feldspar (40 vol%), plagioclase (15 vol%), quartz (40 vol%), and garnet, biotite, kyanite, and rutile (<5 vol%), and displays fine-grained equigranular texture. Granulites are typically surrounded by the granofelses. The ECC shows alternating layers of the individual rock types that are parallel to the S_1 compositional layering, most conspicuous in the banded orthogneiss (Fig. 2A).

Deformation Fabrics

The ECC shows alternating layers/bands of the individual rock types that are parallel to the S_1 compositional layering, most conspicuous in the banded orthogneiss (Fig. 2A). The ECC shows three major structural domains (Fig. 1) that differ in the proportion of individual rock types and deformation styles that fold the S_1

fabrics. Domain A, in the western part of the studied profile, is dominated by banded orthogneiss with rare interlayers of the granofels. Domain B, in the east, displays an equal proportion of granofels and orthogneiss together with migmatites. Domain C consists exclusively of granofels and granulite. In this study, we focus on domains A and B (Figs. 1B, 1C).

There are three major deformation fabrics developed throughout the ECC. The S_1 layering is defined by S-type fabrics of banded orthogneisses and mylonites and parallel lithological boundaries of the alternating rock types (Figs. 3A–3C). In few subdomains that are unaffected by later phases of folding (Fig. 3B), the S_1 fabric is flat or dipping to the south at shallow angles. The S_1 layering is folded by upright open to closed F_2 folds associated with S_2 axial planar cleavage that dips south at steep angles (Figs. 1C, 3A, 3D, and 3E). In domain A, the subvertical S_2 foliation is affected by another generation of asymmetric open to closed chevron upright folds F_3 with northwest-southeast–trending fold axial planes S_3 and subvertical hinges (Figs. 1C and 3E). Resulting fold interference pattern creates curtain folds deforming curved and subhorizontal L_2 lineations and F_2 fold hinges (Fig. 3E).

In domain A, S_1 layering is preserved only locally in isolated zones of banded orthogneiss (Figs. 3A, 3B). These zones are folded by upright open to closed folds, intercalated with narrow channels of granitic melt along both the S_1 layering and S_2 cleavage (Figs. 3A, 3D). The granofels contains leucosome patches and forms isolated layers (maximum 20 cm thick) parallel to the S_1 layering of the banded orthogneisses (Fig. 3B). In domain B, S_1 layering as well as the lithological contacts between individual rock types are
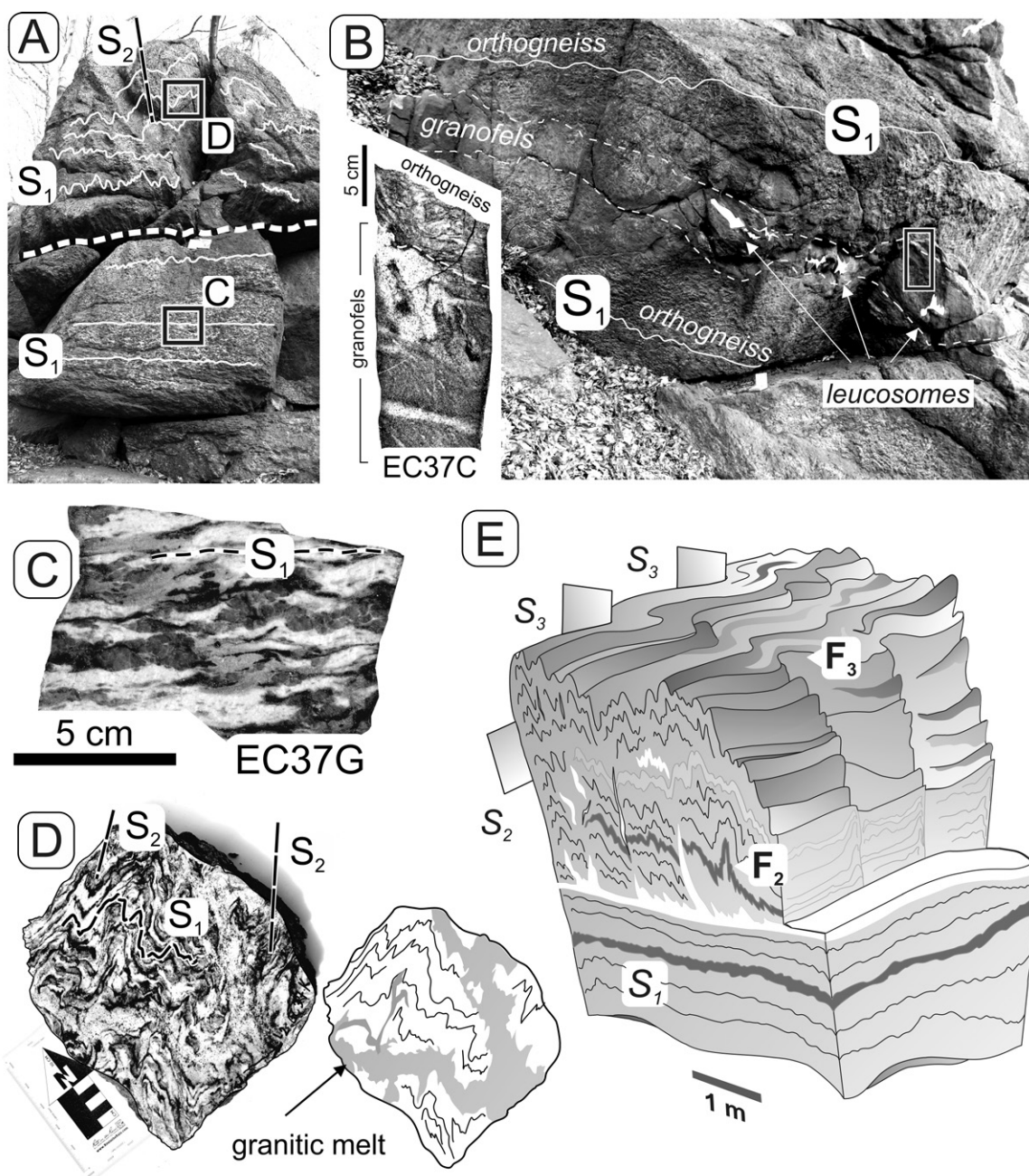
Figure 3. (A, B) Outcrop photographs illustrating the folding style in domain A. The detachment plane between the folded anatectic domain and underlying flat-lying S_1 fabrics is indicated by a thick dashed line in A. Outcrop shown in B is located just 10 m below the outcrop in A and reveals a single, 20-cm-thick granofels layer in banded orthogneisses with flat-lying S_1 fabrics. Note that the S_1 fabrics and the contact between the orthogneisses and the granofels are concordant and both are only slightly crenulated. Location of rock section capturing the contact between the orthogneiss and the granofels (inset) is shown with a black rectangle in B. The rock section in B shows a leucosome patch with biotite-rich restite in the granofels at the contact with the orthogneiss. Another leucosome forms a 1-cm-thick and S_1 parallel layer at the bottom of this rock section. A 7-cm-wide geological compass at the center of A and bottom part of B is shown for scale. **(C)** Section of rock sample collected below the detachment plane shows only slightly crenulated typical S_1 fabrics, with alternating bands of feldspars surrounding lenses of quartz and streaks of mica aggregates. **(D)** Rock section in the folded domain reveals crenulated S_1 fabrics interspersed by granitic melt along both the S_1 fabrics and fold axial planes S_2 (see inset for schematic sketch). **(E)** A schematic block diagram summarizing the outcrop-scale structure, where a granofels layer is shown in dark gray, orthogneiss in light gray and migmatites or granitic melt in white.
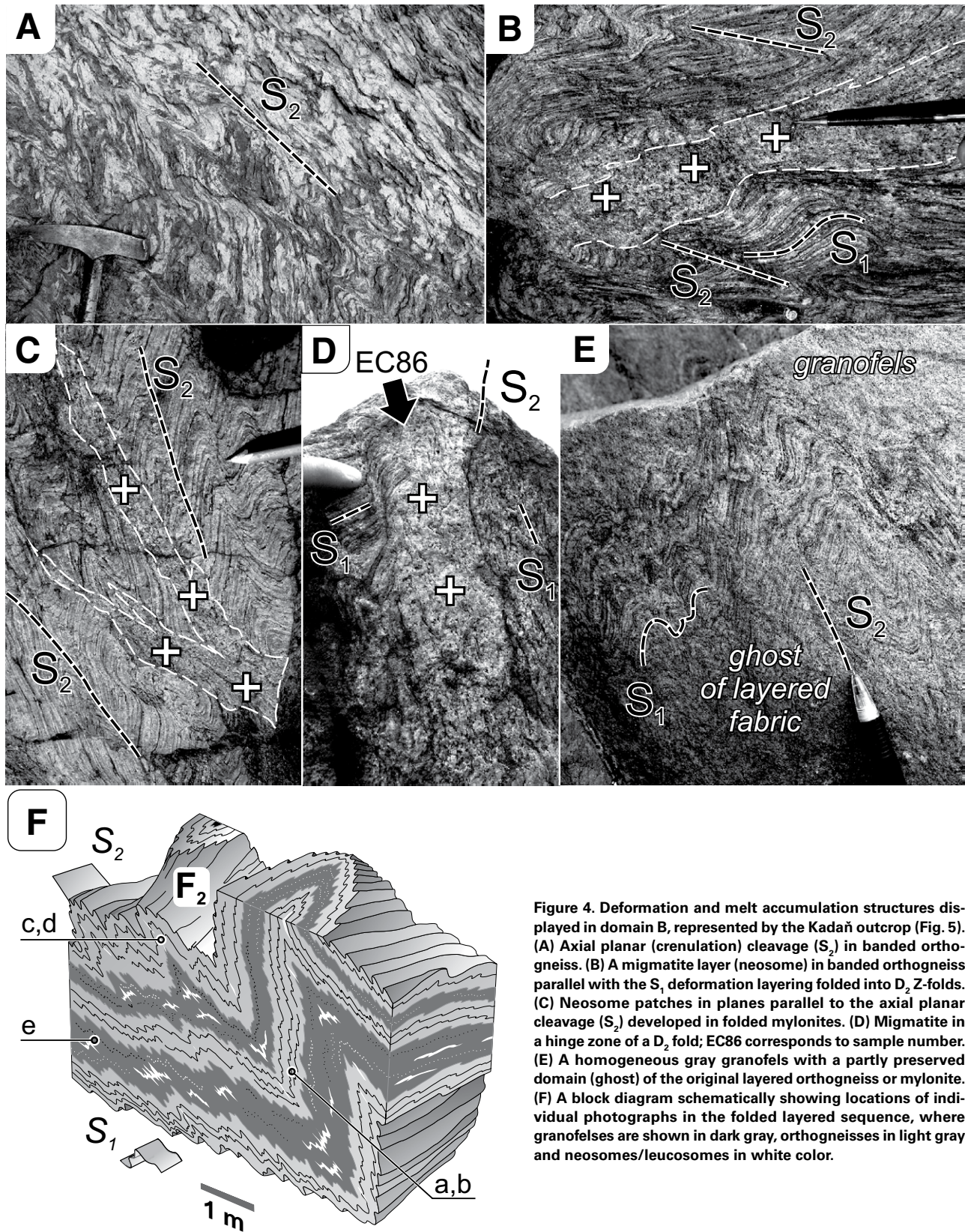
Figure 4. Deformation and melt accumulation structures displayed in domain B, represented by the Kadaň outcrop (Fig. 5). (A) Axial planar (crenulation) cleavage (S_2) in banded orthogneiss. (B) A migmatite layer (neosome) in banded orthogneiss parallel with the S_1 deformation layering folded into D_2 Z-folds. (C) Neosome patches in planes parallel to the axial planar cleavage (S_2) developed in folded mylonites. (D) Migmatite in a hinge zone of a D_2 fold; EC86 corresponds to sample number. (E) A homogeneous gray granofels with a partly preserved domain (ghost) of the original layered orthogneiss or mylonite. (F) A block diagram schematically showing locations of individual photographs in the folded layered sequence, where granofelses are shown in dark gray, orthogneisses in light gray and neosomes/leucosomes in white color.
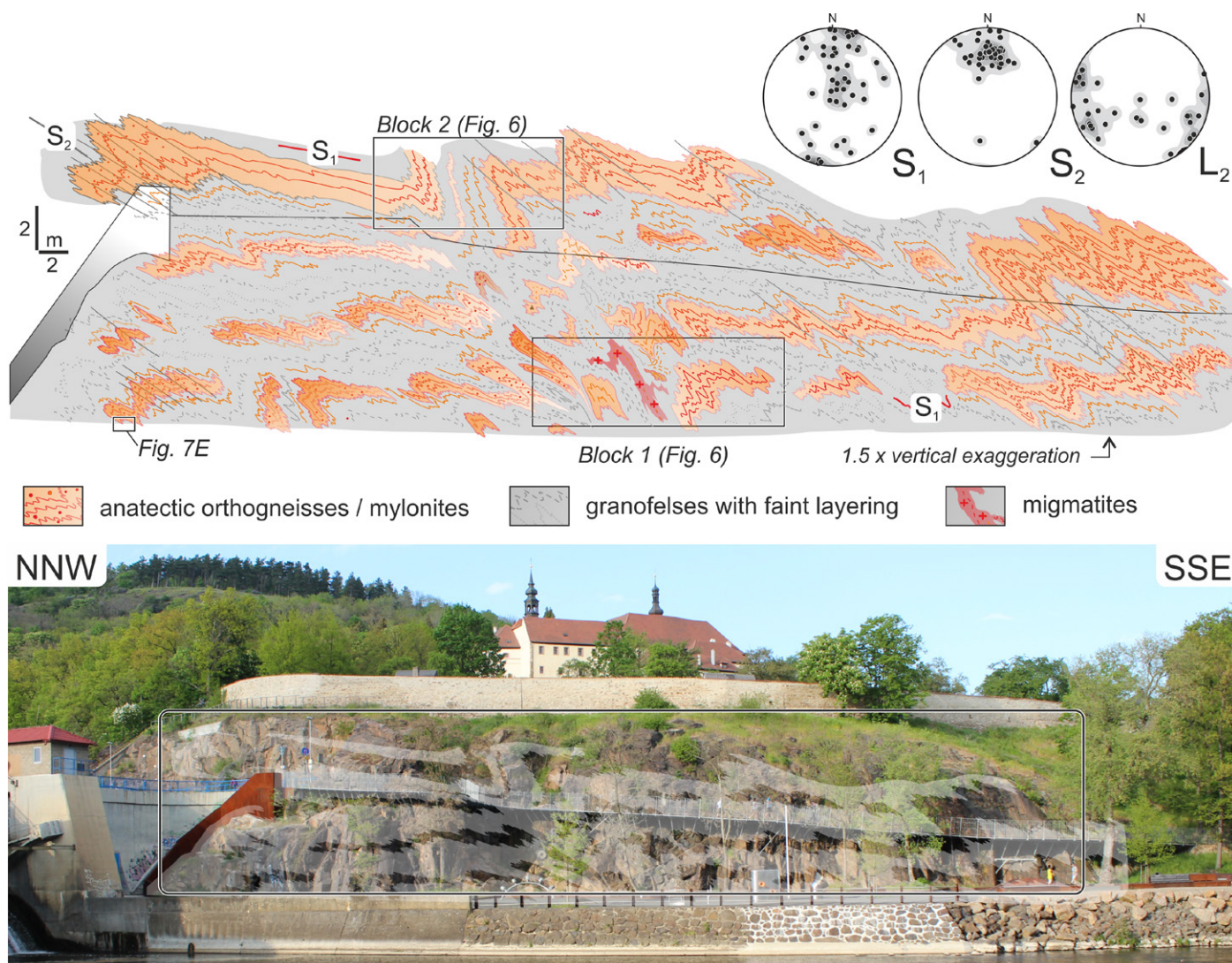
Figure 5. Detailed lithological map of a vertical section of the studied outcrop located in the town of Kadaň at a dam across the Ohře River on its northern bank. Extent of the mapped domain is shown by the black rectangle on the photograph at the bottom. Lower hemisphere equal area stereoplots show poles of measured planar fabrics S_1 and S_2 and directions of L_2 intersection lineations. Middle part of the vertical outcrop is accessible from an elevated pathway (marked by an inclined black line). Note the locations of detailed block diagrams (depicted in Fig. 6) indicated by rectangles and location of an extra slab in the bottom left part of the outcrop (shown in Fig. 7E).

folded by open rounded to closed Z-shaped folds with fold planes and fold axial cleavage (Figs. 4A–4C) dipping south at ~60° (Figs. 1, 4, and 5). The hinge zones of these folds display intense L-type fabrics resulting from the transposition of S_1 by S_2 and formation of L_2 intersection subhorizontal lineation. Some hinges of the D_2 folds in migmatitic orthogneisses or mylonites show patches of neosomes aligned parallel with the fold axial cleavage (Fig. 4D). Toward the west, the S_2 cleavage progressively rotates to steep north-northeast–south-southwest–trending orientation (Fig. 1C). Variations in plunge of both the b-axes of the small crenulation folds and the L_2 intersection lineations indicate strongly noncylindrical shape of these folds (Fig. 4F and stereoplot in Fig. 5).

Macroscopic Relationships of Melt, Rock Types, and Structures

In this study we aim to understand the origin of granofels layers and their role in the exhumation of the entire ECC. Therefore, we have studied in detail the macroscale to microscale deformation pattern and crystallized melt distribution in the granofels layers, as well as in the surrounding banded orthogneiss in the representative outcrop in Kadaň (Fig. 5). This outcrop shows alternating layers (S_1) of banded orthogneisses, migmatites, fine-grained mylonites, and granofelses. The entire rock package was folded by north-verging open to closed Z-shaped rounded to chevron folds (Figs. 5 and 6). These asymmetrical folds have wavelengths

from several decimeters to meters (Fig. 5) with upright short limbs and long limbs, gently dipping to the south. Cusp-like interfaces of granofels locally protruding into the hinge zones of the larger folds suggest that this rock was less competent compared to the banded orthogneiss (Ramsay and Huber, 1987). The folds in the banded orthogneiss display asymmetric parasitic folds (wavelength of 5–10 cm) with axial planar patches of migmatites that consist entirely of neosomes (Figs. 4D and 6).

The estimated volume of former melt (as rare leucosomes, Fig. 4A) in banded orthogneiss ranges between 1 and 5 vol% (Fig. 4A). In the migmatites, the melt stored in neosomes (including the leucosomes) is more abundant (<25 vol%; Fig. 4B) than in the orthogneisses,
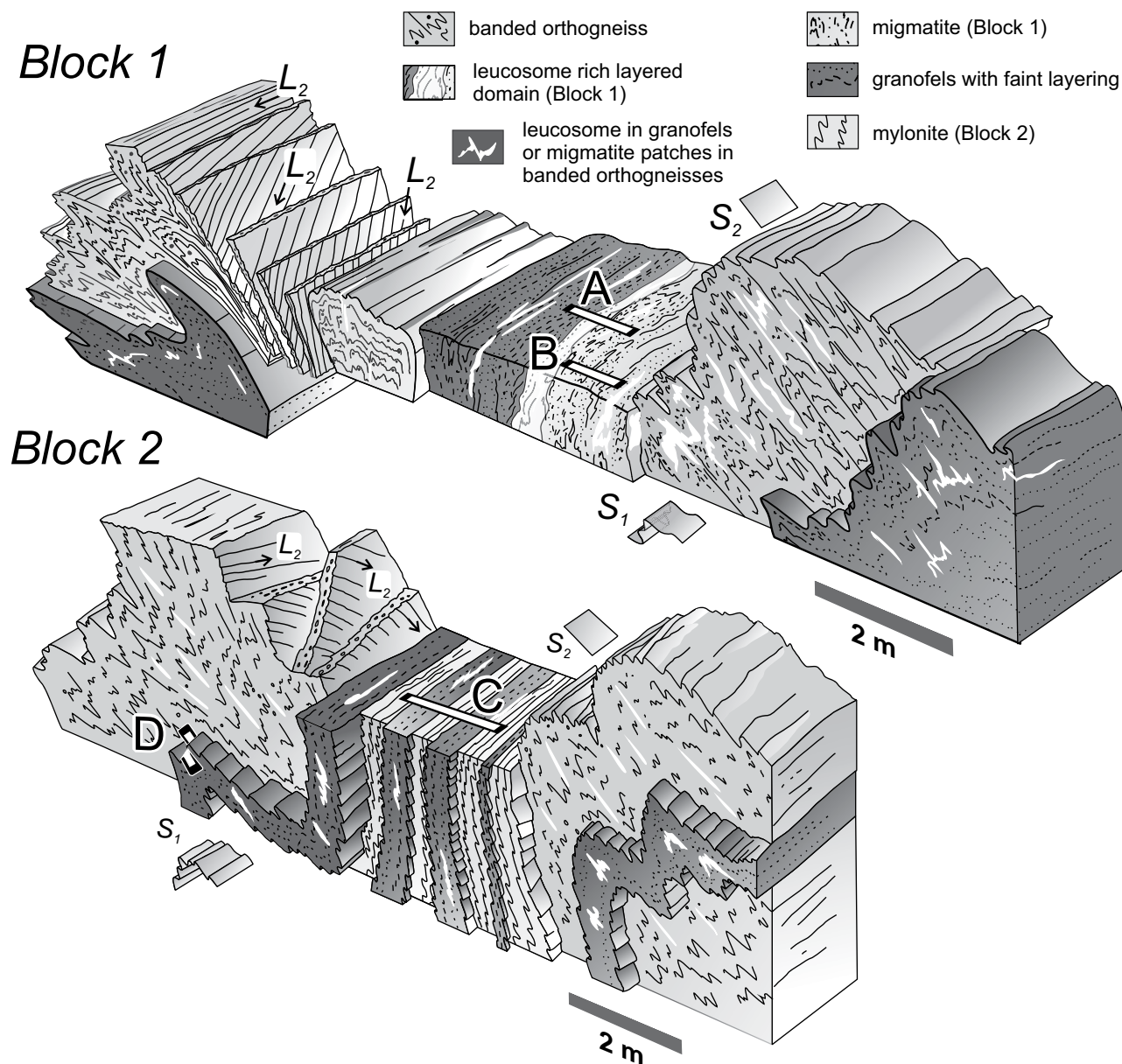
Figure 6. Block diagrams showing the folded lithological contacts, deformation fabrics, and deformed leucosomes in two domains selected for sampling (see Fig. 5 for location). A, B, C and D indicate sampled slab sections presented in Figures 7A–7D, respectively.

and the neosomes form lenses either parallel to S_1 (Figs. 4B and 6) or mark the S_2 axial planar foliation, where they are connected to leucosomes parallel to the S_1 layering (Fig. 4D). The most characteristic features of granofels layers are their diffuse S_1 parallel transitions with the surrounding orthogneisses or mylonites, where the compositional layering typical of the latter rock gradually disappears into the granofels over a distance of ~5–10 cm (Figs. 4E, 7D, and 7E). In thick granofels layers (>2 m), ghosts of crenulated layered fabric can be found (Fig. 4E). These ghosts display faint thin layering in structural continuity with the fabrics of the orthogneisses

in the surroundings of the granofelses. Boundaries of banded orthogneisses and migmatites with the granofelses are locally traced by interconnected network of leucosomes (Fig. 7A). Locally, the hinge zones of the folded granofels layers display a well-developed network of S_1 parallel and axial plane and S_2 parallel leucosomes with estimated proportion of both sets at 15–25 vol% (Fig. 7E). While the S_1 parallel leucosomes typically form isolated lenses, as much as 10 cm long and 1 cm thick, the S_2 axial planar leucosomes are rather continuous and locally intrude the surrounding banded orthogneisses or migmatites (Figs. 7D, 7E). Contacts between these two

discordant sets of leucosomes are gradational, which suggests that they were interconnected and contained melt at the same time (Vanderhaeghe 1999, 2001; Barraud et al., 2004; Vernon and Paterson, 2001; Sawyer, 2008; Kisters et al., 2009; Hall and Kisters, 2012).

MICROSTRUCTURAL OBSERVATIONS: TRANSITION BETWEEN BANDED ORTHOGNEISS AND GRANOFELS

We cut five rock slabs (A–E) from key domains on the Kadaň outcrop and made thin sections of the different rock and leucosome
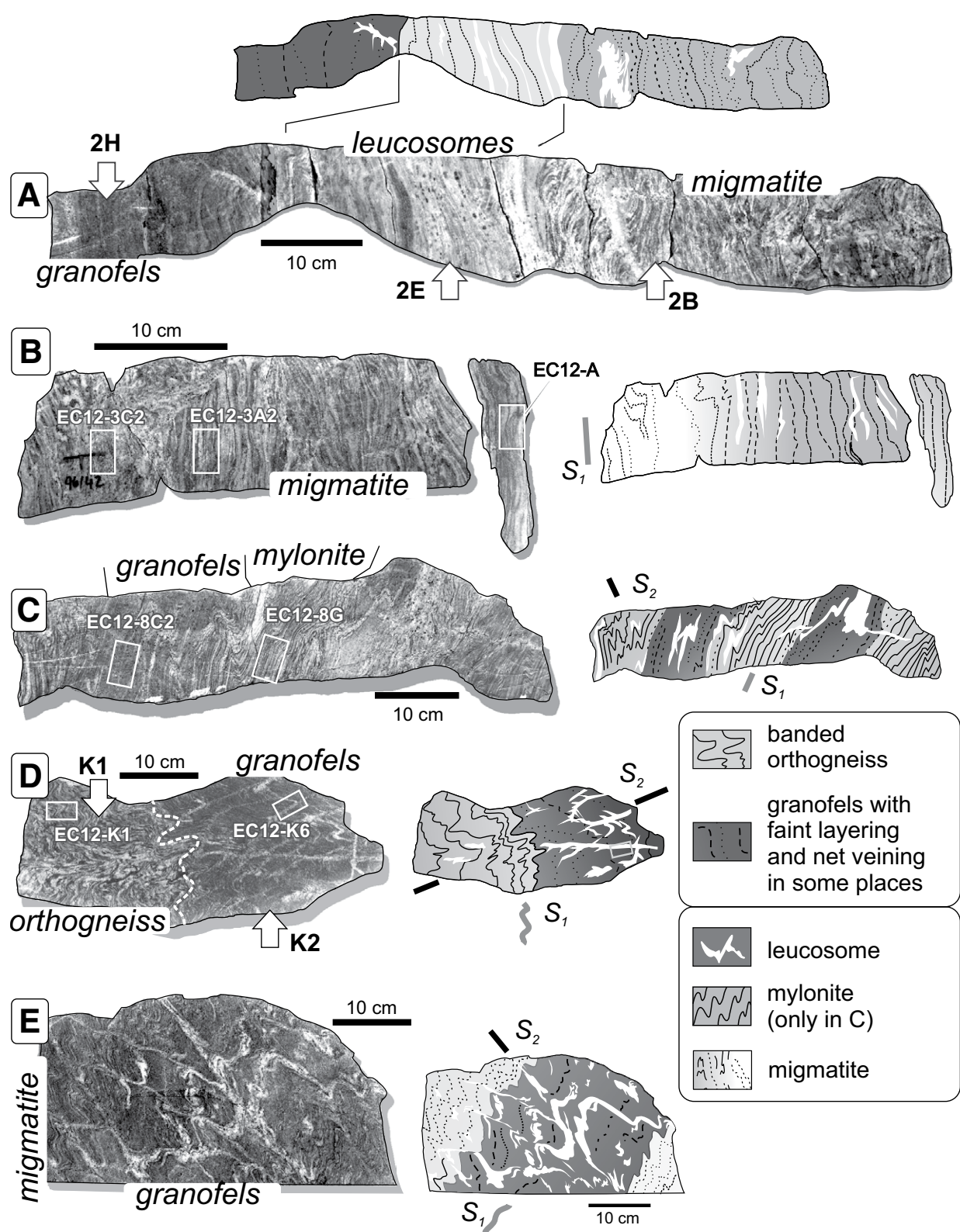
Figure 7. (A–E) Photographs of cut-out slabs and associated interpretative lithological maps with depicted S_1 layering and leucosomes. Locations of thin sections are indicated by white rectangles. Numbered white arrows tagged with sample names indicate lithological types analyzed for bulk-rock chemistry and mass-balance calculations (Fig. 11; DR File; Fig. DR5). (For location of slab E, see the outcrop map in Fig. 5.)

types. Slab A (Fig. 7A) captures a contact between a banded orthogneiss (grading continuously into migmatite) and a granofels, traced by a set of layer-parallel leucosomes. Slab B (Fig. 7B) depicts, from right to left, the disruption of the typical banded orthogneiss by increased anatexis. Slab C (Fig. 7C) represents thinly banded mylonite enclosing two granofels layers. Slab D (Fig. 7D) was taken from a hinge zone of a fold with S_1 crenulations and shows a contact between banded orthogneiss and a granofels, both with leucosomes. Slab E reveals another hinge zone of a fold with a 20-cm-thick granofels layer sandwiched in a fine-grained migmatite (Fig. 7E). In the following subsections, we first detail the microstructural characteristics of the different rock types, then focus on the melt topology interpretation and melt content quantification from the microstructures for the individual rock types (see the DR File for the details of this method). Locations of the thin sections used for the microstructural study are displayed in Figure 7.

Banded Orthogneiss, Mylonite, Migmatite, and Granofels

Banded orthogneiss and mylonite are characterized by monomineralic banding with alternating aggregates of K-feldspar (0.46–0.63 mm grain size; Table 1), plagioclase (0.29–0.57 mm grain size), quartz, and micas (Figs. 8A–8C and 9A). Modal content of feldspars and quartz is 25–36 vol% and 34–50 vol%, respectively (Table 2). Quartz forms elongated aggregates or ribbons with corroded irregular shapes (Figs. 8A, 8C, 8I) that commonly contain polycrystalline feldspar inclusions elongated perpendicular to the layering (Figs. 8A, 8C, 8I). These inclusions show irregular intergrowths of both K-feldspar and plagioclase (anorthite, An_{0-5}). Feldspar bands reveal an equigranular mosaic of grains with straight mutual boundaries and contain numerous plagioclase, quartz, and K-feldspar inclusions. K-feldspar bands typically contain interstitial plagioclase and quartz grains. Plagioclase forms either thin narrow films along or across the K-feldspar boundaries (Fig. 9A) or larger irregular pockets with lobate boundaries (Figs. 8A–8C and 9A). Quartz

forms rounded grains at triple point junctions (Fig. 9A). Similarly, plagioclase bands reveal interstitial K-feldspar films or pools and quartz grains (Fig. 8C). Plagioclase grains with interstitial K-feldspar along their boundaries show clear zoning, with oligoclase cores (An_{10-15}) and thin albite rims (An_{0-5}). Micas (14%) form euhedral grains, decussate microstructure and trace the plagioclase bands. Small rounded garnets are associated with biotite grains.

Migmatites are characterized by continuous disintegration of the alternating layers of K-feldspar, plagioclase, quartz, and micas (Figs. 8D, 8E, 9B, and 9C) due to progressively increasing amount of interstitial grains of unlike phases. With the increasing disintegration, the monomineralic banding becomes disrupted and only ghost relics of original monomineralic aggregates are preserved (Fig. 8E). Feldspar and quartz aggregates show highly irregular corroded shapes and grain boundaries that are traced by a polyphase fine-grained mixture of albite and/or oligoclase, quartz, and K-feldspar grains (Fig. 9B, 9C). Garnet grains are large, atoll shaped, and contain pools formed by irregularly intergrown grains of K-feldspar, plagioclase, and quartz (Fig. 9C). Muscovite is dispersed throughout the matrix. Increasing degrees of migmatization captured in the sequence of samples EC12-A, EC12-3A2, and EC12-3C2 (Figs. 8A, 8D, 8E; Table 3) are associated with decreasing content of micas from ~20 vol% to 15 vol%. The interstitial grains form irregular pools with tortuous appendices that sometimes line boundaries of several grains in the direction perpendicular to the residual layering (Figs. 9B, 9C). The pools are filled by a mixture of fine-grained anhedral K-feldspar, albite, and quartz. Albite grains in the pools locally form thick overgrowths on the residual oligoclase grains. Some of the pools formed by K-feldspar extend into pockets protruding into residual plagioclase (Figs. 8E, 9B). Other pools contain isolated inclusions or clusters of irregularly shaped, new grains of albite and quartz (Fig. 9C).

Granofels is characterized by fine-grained granoblastic aggregate of feldspars, quartz, and micas (Figs. 8F, 8G, and 9D; Tables 2, 3). Locally, K-feldspar grains form aggregates

parallel to the S_1 fabric (Fig. 8F, 8G). Similarly, feldspars and quartz show a weak shape preferred orientation (SPO) parallel with the S_1 layering. K-feldspar and quartz grains are lined by irregular aggregates of quartz, plagioclase, and K-feldspar. Granofels sandwiched between mylonites (EC12-8C2 in Fig. 7C) commonly contains K-feldspar grains that have transgranular cracks oriented at high angles to the faint layering; some are filled by interstitial feldspar, mica, or circular grains of quartz (Fig. 9D). Muscovite crystals have straight boundaries, are dispersed homogeneously throughout the matrix, and are mostly oriented parallel to the S_1 fabric. Garnet grains (<5 mm) are strongly corroded and embayed by a mixture of anhedral feldspars and quartz. Kyanite (<0.2 mm) may be present in matrix as relicts enveloped by plagioclase.

Crystallized Melt Volume and Topology

Many have summarized criteria for recognition of former melt at grain scale in metamorphic rocks (e.g., Závada et al., 2007; Holness and Sawyer, 2008; Hasalová et al., 2008b, 2011). Using these criteria we interpret the described interstitial films, and pools in the banded orthogneiss, migmatite, and granofels, as former crystallized melt. Estimated melt proportions from the phase maps range between 5 and 16 vol%, are highest in the migmatites and granofels (Table 2), and roughly correlate with the mesoscale estimates based on the proportion of leucosomes on the sampled slabs (Fig. 7). Leucosomes are regarded as macroscopically visible crystallized melt that accumulated in structural mechanical anisotropies (S_1 and S_2 fold cleavage). Leucosomes in the migmatites and granofelses consist of ~0.5 mm large anhedral grains of feldspars and quartz and are considered compositionally equivalent to the microscopic pools in the migmatites. These leucosomes do not contain any pools comparable to those in the migmatites. We have calculated P-T conditions for the banded orthogneiss (pseudosection modeling using Thermocalc, www.thermocalc.com/; data presented in the DR File; Fig. DR4) that indicate melting conditions of ~720–800 °C and 13 kbar. Using the upper temperature limit of 800 °C (at 13 kbar), maximum

TABLE 1. EQUAL AREA DIAMETERS AND AXIAL RATIOS OF BOTH FELDSPARS IN STUDIED SAMPLES (STATISTICS OF MINIMUM 100 GRAINS)

		Orthogneiss EC12-A	Migmatite EC12-3A2	Migmatite EC12-3C2	Mylonite EC12-8G	Granofels EC12-8C2	Orthogneiss EC12-K1	Granofels EC12-K6
EAD (mm)	Ksp	0.63	0.60	0.56	0.46	0.28	0.52	0.34
	Pl	0.44	0.40	0.57	0.29	0.27	0.40	0.27
Axial ratio	Ksp	1.49	1.52	1.47	1.54	1.57	1.46	1.56
	Pl	1.47	1.42	1.43	1.49	1.48	1.38	1.43

Note: EAD—equal area diameters; Ksp—potassium feldspar; Pl—plagioclase; green—samples with relatively coarser grain size; orange—fine-grained samples.
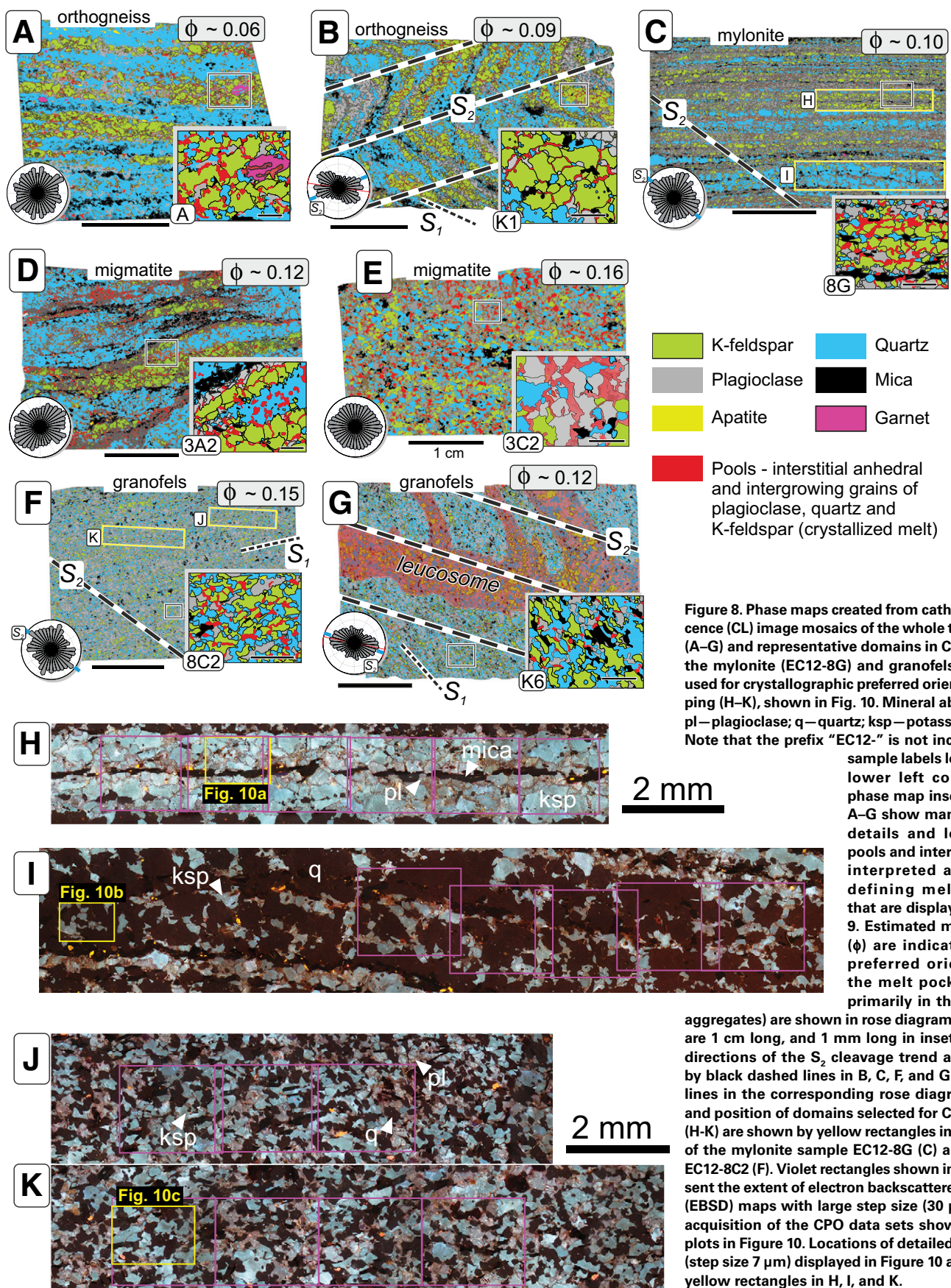
Figure 8. Phase maps created from cathodoluminescence (CL) image mosaics of the whole thin sections. (A–G) and representative domains in CL mosaics of the mylonite (EC12-8G) and granofels (EC12-8C2) used for crystallographic preferred orientation mapping (H–K), shown in Fig. 10. Mineral abbreviations: pl—plagioclase; q—quartz; ksp—potassium feldspar. Note that the prefix "EC12-" is not included in the sample labels located in the lower left corner of the phase map insets. Insets in A–G show manually traced details and locations of pools and interstitial grains interpreted as melt and defining melt topology that are displayed in Figure 9. Estimated melt volumes (ϕ) are indicated. Shape-preferred orientation of the melt pockets (traced primarily in the K-feldspar aggregates) are shown in rose diagrams. Scale bars are 1 cm long, and 1 mm long in insets. Note that directions of the S_2 cleavage trend are indicated by black dashed lines in B, C, F, and G and by blue lines in the corresponding rose diagrams. Extent and position of domains selected for CPO mapping (H-K) are shown by yellow rectangles in phase maps of the mylonite sample EC12-8G (C) and granofels EC12-8C2 (F). Violet rectangles shown in (H–K) represent the extent of electron backscattered diffraction (EBSD) maps with large step size (30 μm) used for acquisition of the CPO data sets shown in stereoplots in Figure 10. Locations of detailed EBSD maps (step size 7 μm) displayed in Figure 10 are shown by yellow rectangles in H, I, and K.
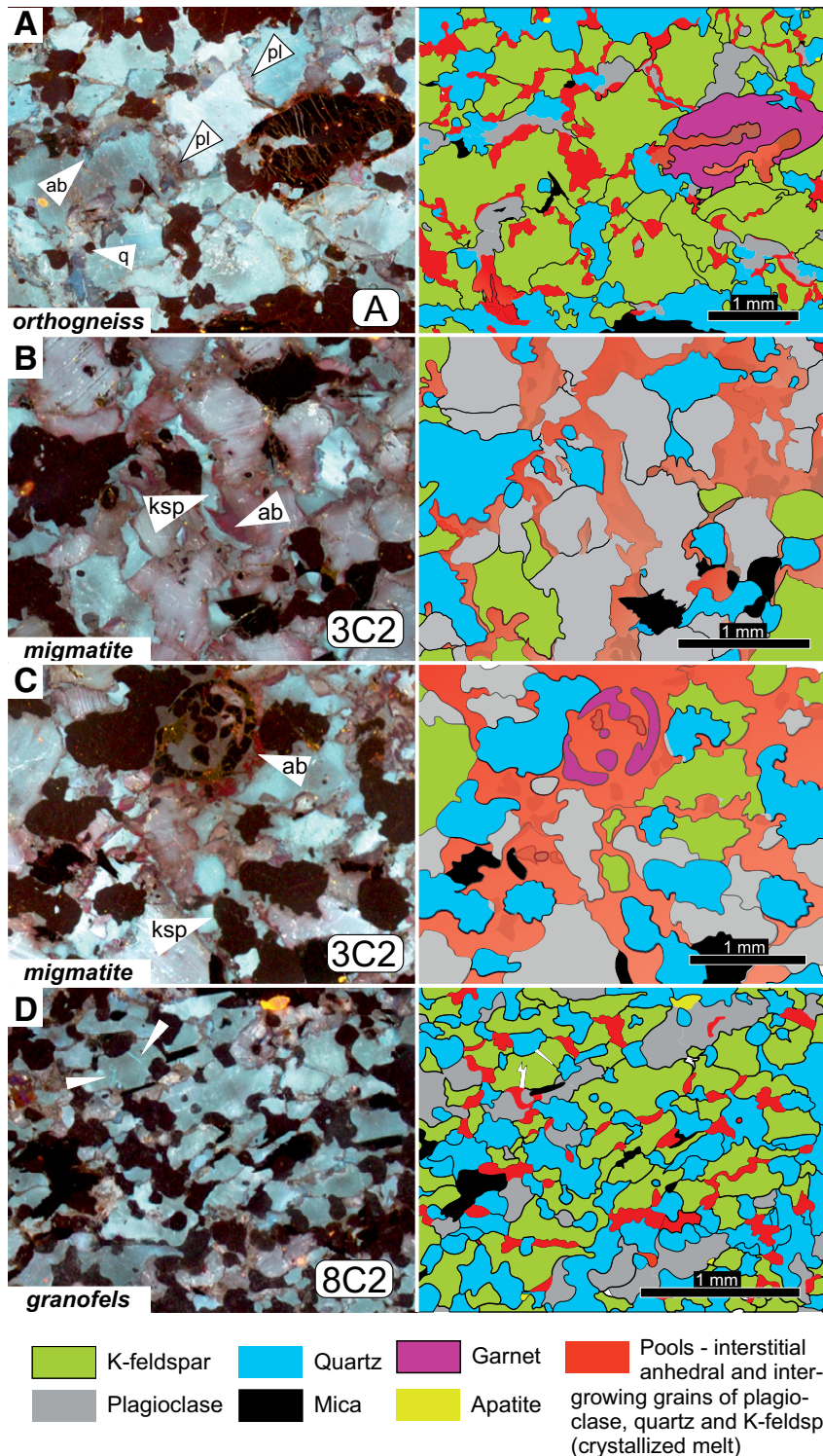
Figure 9. Optical cathodoluminescence images of selected representative microstructures (on left) and line drawings (on right) showing distribution of individual phases and interpreted melt topology. Line drawings and related images correspond to small insets in Figure 8 (A–G). Mineral abbreviations: pl—plagioclase; q—quartz; ksp—potassium feldspar; ab—albite. Note that the prefix "EC12-" is not included in the sample labels located in the lower right corner of the CL images. **(A)** The orthogneiss shows thick interstitial grains in K-feldspar bands and corroded shape of garnet showing embayments and holes, where melt crystallized as quartz, K-feldspar, and plagioclase. **(B, C)** Migmatite reveals large pools in the granular framework, highly corroded garnet crystals and pools marked by irregular inclusions of albites or thick albite rims overgrowing the plagioclase. **(D)** Granofels reveals small pools and transgranular cracks in K-feldspar, indicated by white triangles.

melt content produced in banded orthogneiss is <~6 vol% (DR File).

SPO of Melt Pockets

The interstitial grains and/or films in the banded orthogneisses and the migmatite either do not show any SPO or very weak SPO parallel to layering (Figs. 8A, 8D, 8E). The SPO of the melt pockets is typically developed in the crenulated and axial parts of the folds (Fig. 8B). In these parts, the orthogneisses show melt pockets forming two maxima aligned at high angles to the layering in both limbs, one of them close to the fold axial cleavage S_2 (Fig. 8B). The granofels sample EC12-K6 from the crenulated fold hinge zone reveals an asymmetric SPO pattern with the major maximum again in the direction of axial cleavage S_2 (Fig. 8G). Similarly, in the mylonite sample EC12-8G and adjacent granofels sample EC12-8C2 (Figs. 8C, 8F), the SPO pattern of melt pockets shows a major maximum parallel with the axial planar cleavage S_2.

Crystallographic Fabric (CPO) of the Mylonite and Adjacent Granofels

In order to define the dominant deformation mechanisms and evaluate the mechanical coupling of grains that form the solid framework in melt-bearing rocks, the crystallographic orientation of the major phases (K-feldspar, plagioclase, quartz) was measured in mylonite (sample EC12-8G) and adjacent granofels (sample EC12-8C2) (Fig. 10).

In the mylonite sample, the crystallographic preferred orientation (CPO) of K-feldspar measured in a K-feldspar band with subordinate interstitial plagioclase (Fig. 10A) reveals a relatively strong CPO fabric marked by J-index ~ 1.66 and a distinct submaxima of poles to (010) at the periphery of the diagram, centered 30°–40° and 20° inward, in the first and third quadrant, respectively. Two submaxima of [001] directions mark the periphery of the stereoplot in the first and fourth quadrant; another small maximum is subparallel to L_2. The [100] directions display an incomplete girdle that crosses the center of the diagram at a high angle to the S_1 foliation. This diffuse girdle is marked by a strong submaximum between the second and third quadrant at 50° inward from the periphery. The [101] directions form a strong maximum near the center of the diagram, roughly parallel to both the foliation and lineation L_2. Another submaximum of this direction is located in the second quadrant.

Interstitial K-feldspar grains (Fig. 10B) measured in the quartz-dominated band of the mylonite (sample EC12-8G) display higher intensity fabrics (J-index ~ 1.71) than for the

TABLE 2. MODAL CONTENT OF MAJOR PHASES AND CRYSTALLIZED INTERSTITIAL MELT QUANTIFIED USING IMAGE ANALYSIS COMBINED WITH MANUAL TRACING OF CATHODOLUMINESCENCE IMAGES

Rock type	Orthogneiss	Migmatite	Migmatite	Mylonite	Granofels	Orthogneiss	Granofels
Sample	EC12-A	EC12-3A2	EC12-3C2	EC12-8G	EC12-8C2	EC12-K1	EC12-K6
Quartz	50.3	39.9	26.4	33.9	29.8	36.1	31.0
K-feldspar	23.4	13.1	25.2	36.2	21.2	25.0	25.0
Plagioclase	12.9	11.3	16.8	14.2	18.1	20.4	15.6
Micas	7.3	12.9	7.0	5.5	15.1	5.8	16.1
Apatite	0.5	0.4	0.1	0.4	0.8	0.3	0.3
Melt	5.6	12.5	16.0	9.8	15.0	8.8	12.0
Altered	0.0	9.9	8.6	–	–	3.6	–
Total	100.0	100.0	100.0	100.0	100.0	100.0	100.0

Note: Modal analyses are in volume percent. Corresponding phase maps are shown in Figure 8A–G. Dash indicates no data.

TABLE 3. MODAL ANALYSES OF MAJOR PHASES FROM IMAGE ANALYSIS OF COMPOSITIONAL MAPS

Rock type	Sample	ksp	pl	q	g	bi	mu	ky	ap	Mica total
Orthogneiss	EC37G	11.88	44.59	28.66	0.78	6.31	7.26	0.00	0.52	13.57
Granofels	EC37C	11.58	30.67	36.19	1.24	4.61	15.38	0.00	0.33	19.99
Orthogneiss	EC12-K1	27.67	17.76	40.07	0.33	3.51	10.38	0.00	0.28	13.89
Granofels	EC12-K6	27.12	20.06	34.92	0.57	2.47	14.53	0.00	0.34	17.00
Mylonite	EC12-8G	26.07	22.58	35.87	1.07	3.05	10.96	0.00	0.41	14.00
Granofels	EC12-8C2	27.63	22.50	33.72	1.92	3.12	10.81	0.00	0.30	13.94
Orthogneiss	EC12-A	27.29	10.55	39.93	0.87	2.43	18.25	0.00	0.68	20.68
Migmatite	EC12-3A2	22.29	19.60	39.47	0.31	2.38	15.61	0.00	0.33	17.99
Migmatite	EC12-3C2	22.54	33.14	28.48	0.55	4.51	10.41	0.00	0.36	14.92

Note: Modal analyses are in volume percent. See the Methodology section in text for technical specifications of the device used for acquisition of the compositional maps. EC37 and EC12 in the sample name prefix correspond to the sampled localities 1 and 2 indicated in Figure 1 and shown in Figures 3 and 7, respectively. Mineral abbreviations: ksp—potassium feldspar; pl—plagioclase; q—quartz; g—garnet; bi—biotite; mu—muscovite; ky—kyanite; ap—apatite.

large grains of the K-feldspar rich band (Fig. 10A). These grains reveal broad single maxima for all crystallographic directions. Poles to (010) planes show a single strong maximum in the first quadrant; [001] and [101] reveal maxima nearly within the foliation plane. While the [101] submaxima are nearly perpendicular to L_2, [001] is centered ~30° inward between the third and fourth quadrant. Directions [100] reveal a maximum on the periphery of the diagram in the second and fourth quadrants that stretches to an incomplete girdle at a high angle to the foliation plane. CPO of quartz grains measured in quartz bands (Fig. 10B) reveals strong fabrics (J-index ~ 1.83), defined by well-constrained maxima of the poles to (0001) close to the foliation pole and girdles defined by poles to the planes {10–10} and {11–20} that are parallel to the foliation plane.

Plagioclase measured in the K-feldspar–dominated band (Fig. 10A) reveals a high-intensity fabric (J-index ~ 2.33) marked by maxima of (010) poles in the third quadrant at ~60° from the periphery of the diagram and a smaller submaximum on the periphery of the fourth quadrant rotated 20° clockwise with respect to the foliation plane. The [001] directions reveal discrete submaxima in the first and between third and fourth quadrant. Directions [101] show single maximum located between the second and third quadrant, rotated ~50° inward from the periphery, and [100] directions show a maximum on the periphery of the diagram, rotated ~25° anticlockwise with respect to the foliation plane pole.

In the granofels sample (sample EC12-8C2) (Fig. 10C), the K-feldspar displays lower intensity fabrics (J-index ~ 1.45) than the band forming K-feldspar (Fig. 10A) and interstitial K-feldspar in quartz aggregates in the mylonite sample EC12-8G (Fig. 10B). The K-feldspar fabric pattern in the granofels is comparable to that of interstitial feldspar in quartz of the mylonite EC12-8G (Fig. 10B): well-defined maximum of [100] directions that is perpendicular to the foliation and stretches to an incomplete girdle at high angle to the foliation, and a broad point maximum of [001] that is nearly perpendicular to the lineation L_2, within the foliation plane. Directions [101] form an elongated maximum between the third and fourth quadrant, while poles to (010) planes form a single maximum near the periphery between the second and third quadrant, centered 20° inward, that stretches to

an incomplete girdle perpendicular to the foliation. Plagioclase reveals two distinct submaxima of [001] directions in the foliation plane that are perpendicular and parallel, respectively, to the L_2. Poles to (010) planes show a single maximum in the foliation plane perpendicular to the L_2. While the directions [101] show single maximum between the second and third quadrant, [100] directions are marked by several submaxima in the center of the diagram, in the second quadrant and between the first and fourth quadrants, rotated 20° inward. Fabric intensity of the plagioclase in the granofels is high (J-index ~ 2.65) and maxima of the [101] are identical to those for stereoplots of interstitial plagioclase in mylonitic K-feldspar bands (Figs. 10A, 10C). Quartz in granofels (Fig. 10C) shows lower fabric intensity (J-index ~ 1.19) than in the mylonitic quartz bands (Fig. 10B) and displays a single maximum of c-axes at the periphery of the diagram in fourth quadrant, accompanied by a broad and broken girdle of {10–10} and {11–20} axes elongated within a plane rotated anticlockwise at 45°, with respect to the foliation plane.

Whole-Rock Geochemistry

To test the relative mobility of melt and/or fluids between the different rock types, we have compared their element budgets using bulk-rock geochemistry (Lonka et al., 1998; Hasalová et al., 2008c; Oliot et al., 2014) (Fig. 11; Fig. DR5). In addition, we have evaluated possible differences in composition of S_1 and S_2 parallel leucosomes (Fig. 11B). Orthogneisses and migmatites (four samples) and granofelses (four samples) are essentially compositionally similar (Fig. 11A), particularly in the major elements (Fig. 11C). Granofels is slightly depleted in FeO, MgO, TiO_2, and Al_2O_3 as well as in high field strength elements (HFSEs) (Fig. 11D). The leucosomes display depletion with respect to the banded orthogneiss (sample K1, Fig. 7D) in a wide range of incompatible elements (primarily the rare earth elements, REEs, and Y, Th, U, and Zr), as well as Ti (Fig. 11B; DR File, Fig. DR5d). The migmatite, marked by leucosomes accumulated along the S_2 cleavage (EC86, Fig. 4D), as compared to banded orthogneiss K1, shows a similar range of depleted elements (REEs, Ca, Mg, Ti, Fe^{3+}, Cs); however, this depletion is less significant than that for the leucosomes in the granofelses. In contrast, this migmatite is enriched in U, Ni, Rb, as well as As, Pb, and Mn (Fig. 11B; Fig. DR5c). Leucosome samples (2E and $S_1 + S_2$ leucosomes) and the migmatite in the S_2 cleavage (EC86) reveal depletion in TiO_2 and MgO, although the content of all the other major oxides is similar (DR File, Figs. DR5b, 5d).
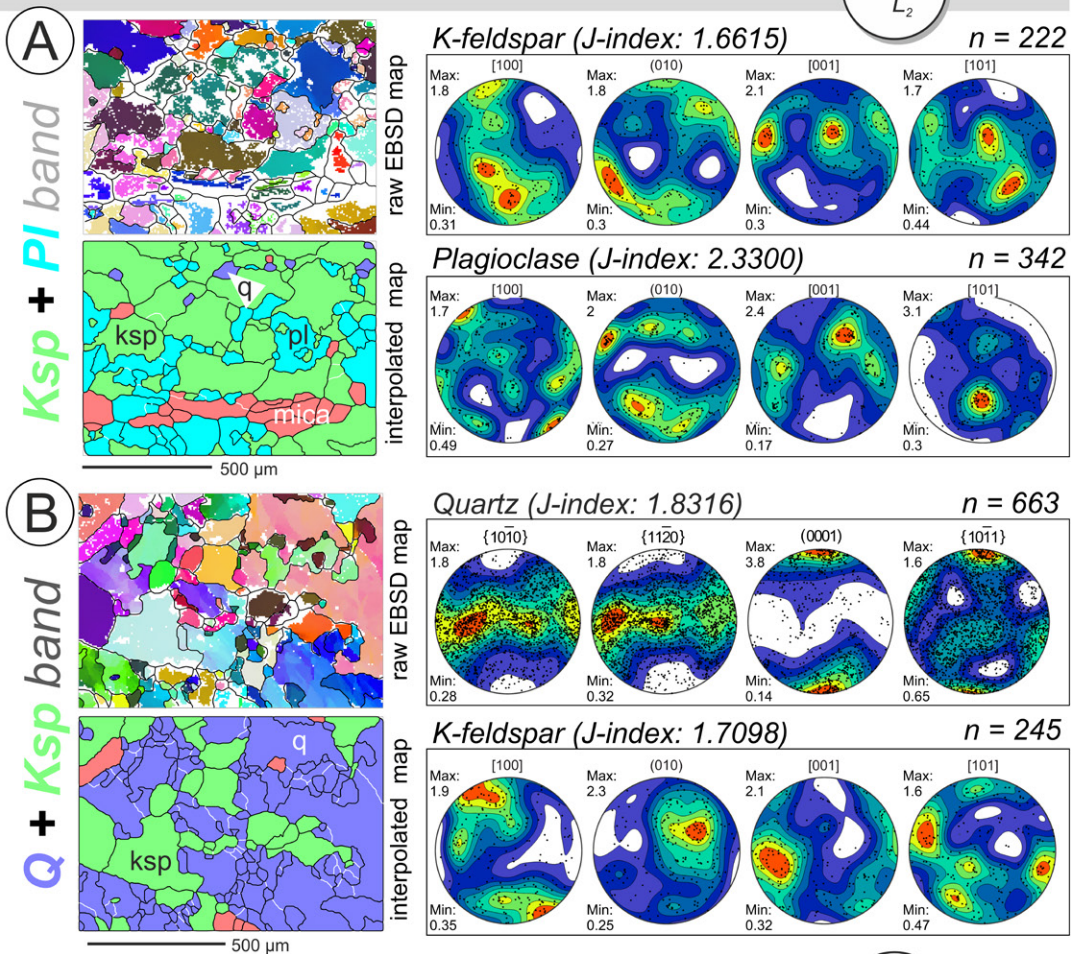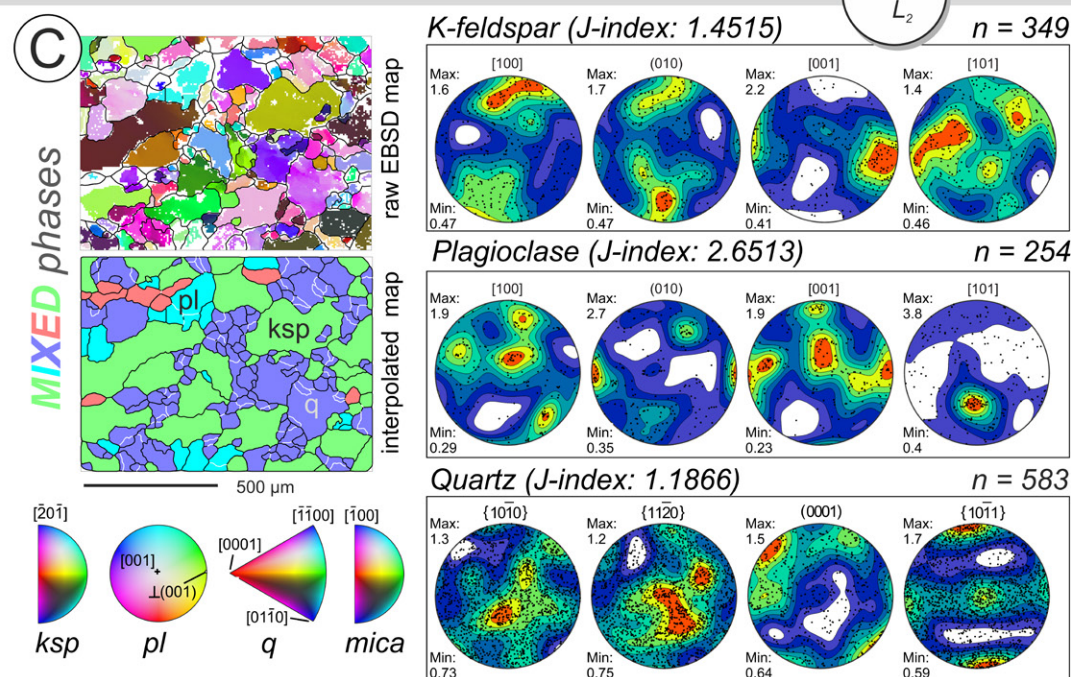
Figure 10. Representative raw electron backscattered diffraction (EBSD) maps with removed bad data and nonindexed points (white pixels) shown alongside the corresponding interpolated phase and grain boundary maps and equal area, upper hemisphere stereographic projections of crystallographic preferred orientation (CPO) for specific microstructural domains in the mylonite (EC12-8G) and the granofels (EC12-8C2) samples. Mineral abbreviations: pl—plagioclase; q—quartz; ksp—potassium feldspar. Max.—maximum; Min.—minimum. Grain boundaries, defined by 10° misorientation angle, are shown by black contours in the raw and interpolated EBSD maps. Subgrain boundaries, defined by 2° misorientation angle, are shown by white contours in interpolated maps. Note that the CPOs in stereographic diagrams display data collected in 11 and 7 maps, respectively, for the EC12-8G and EC12-8C2 samples (see Fig. 8 for locations of these maps). Mylonite sample EC12-8G is represented by two subdomains representing a K-feldspar–dominated band with interstitial plagioclase (A) and quartz band with interstitial K-feldspar (B). (C) Granofels is shown only in one set of stereoplots, because its fine-grained structure is homogeneous. Total number of measured grains (n) in each figure is specified for each phase. The raw EBSD maps are colored according to the inverse pole figure color schemes (bottom left in C) marking the position of the right horizontal direction with respect to the crystallographic orientation of the individual grains. Points in the pole figures represent integrated orientation of individual grains, while the underlying contours represent the multiples of uniform distribution of orientation distribution function. The J-index indicates the strength of the CPO. Thin sections are oriented perpendicular to the S_1 layering and intersection lineation L_2, because lineations L_1, associated with the S_1 planes were not identified. At the same time, the formation of S_1 and subsequent fold axial cleavage S_2 are interpreted to develop in the kinematic continuity, implying that the L_1 transport direction was perpendicular to intersection lineation L_2.
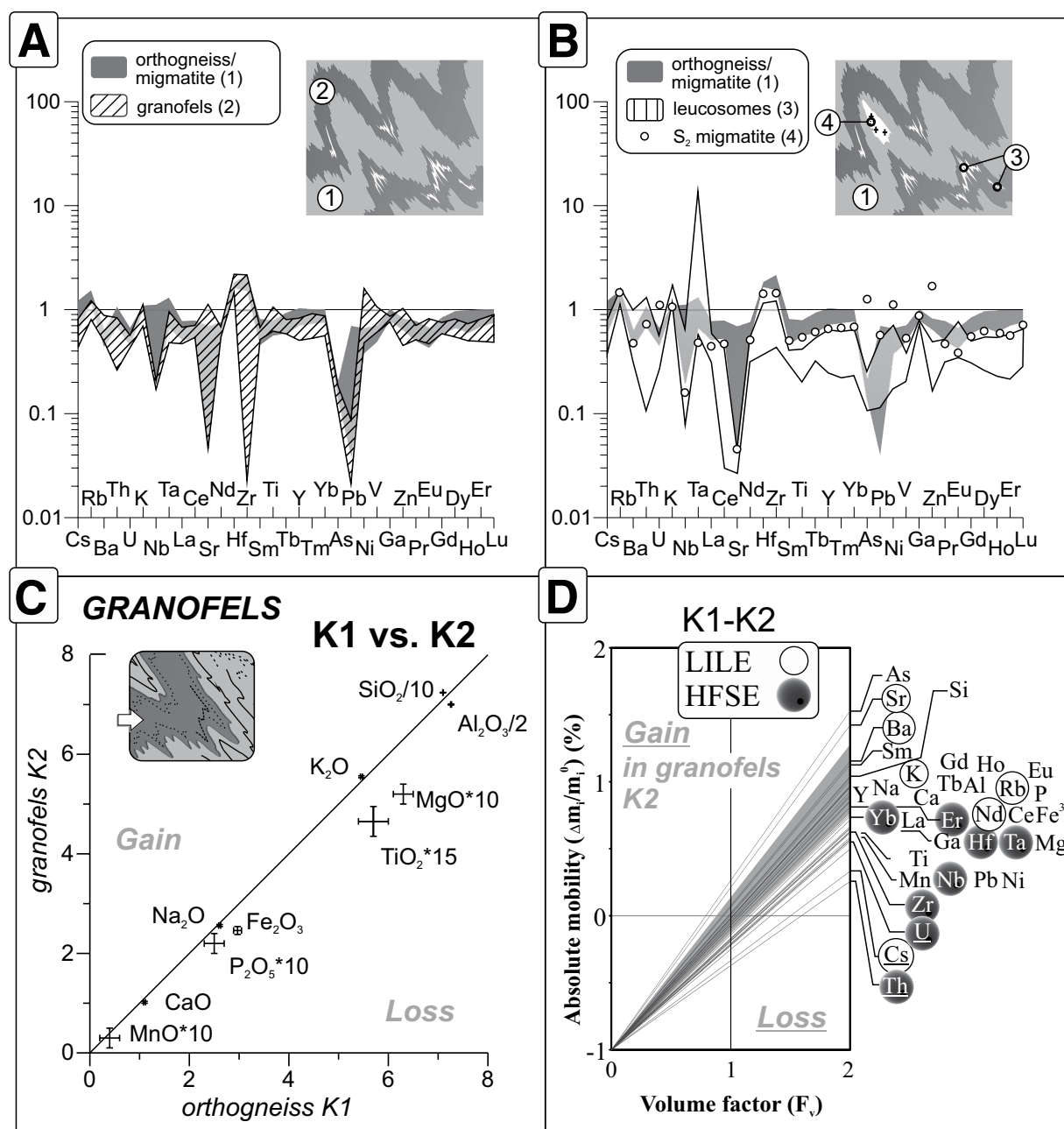
Figure 11. Compositional variations between the different studied anatectic rock types and leucosomes presented in the spiderplots (A, B) normalized by a banded orthogneiss sample lacking signs of macroscopic partial melting (sample EC27 from domain A, Fig. 1; composition of plotted samples in DR File; Table DR2). Note that the granofelses and orthogneisses in A and B are represented by four samples in each group. Leucosomes show a range of compositions measured for five samples; one sample is represented by intergrowing leucosomes shown in Figure 7 (sample 2E); a pair of samples was drilled from S_1 parallel and another pair from S_2 parallel leucosomes, respectively, in both slabs D and E (see Figs. 7D, 7E). Isocon diagram (C) of Grant (1986) and diagrams of Potdevin (D) (Potdevin and Marquer, 1987; López-Moro, 2012) illustrate the loss-gain relationships for a range of elements for banded orthogneiss K1 and adjacent granofels K2 (see Fig. 7 for their location). Relative gain or loss of mass Δm_i is normalized by the initial mass m_0^i in the volume-composition diagrams. Shaded area corresponds to an artificial fluctuation range, for which the elements are considered relatively immobile. While the isocon diagram (Grant, 1986) displays the comparison of only major elements, the composition-volume diagram (diagrams of Potdevin; Gresens, 1967; Potdevin and Marquer, 1987) shows the selected 35 major and minor elements, including the rare earth elements. Note that the detailed results of composition-volume calculations after Gresens (1967) for other samples shown in Figures 4D and 7A are presented in the DR File (Fig. DR5). HFSE—high field strength elements; LILE—large ion lithophile elements.

DISCUSSION

We focus here on the genesis of the granofels layers and we propose their origin through a feedback process linking strain localization and melt flow. Subsequently, we discuss possible deformation mechanisms related to complex melt-solid grains interactions during subduction of continental crust. We discuss the significance of asymmetrical folds and axial leucosomes and their potential role for the exhumation of the entire HP to UHP sequence.

Relationship Between Deformation and Melt Flow

The thickness of the granofels layers and their abundance progressively increase from domain A through B to C, where the granofels alternates with felsic granulites only (Fig. 1). This trend of increasing abundance of granofels at the expense of the layered orthogneiss is further discussed in terms of deformation mechanisms, the mode of grain-scale melt percolation, and pressure gradient.

Are Granofelses Cores of High Strain Zones?

The main question addressed in this paper is related to the origin of the granofels layers with regard to surrounding orthogneiss. Theoretically, there are four possibilities to explain the nature of granofels layers: (1) granofels represents rock of different protolith part of a compositionally heterogeneous crust; (2) granofels is a granodioritic dike intruding the deformed sequence parallel to the main anisotropy; (3) granofels is a diatexite representing a cumulate after melt extraction along the stress gradients; or (4) granofels is a core of a zone of increased strain accommodated by granular flow and porous melt migration that reflects strain partitioning in metagranitoid crust.

Numerous field observations show that the equigranular fine-grained granofels gradually passes to the mylonites and banded orthogneisses, creating characteristic diffuse transitions (Figs. 4E, 7C–7E). Such a diffuse sequence of rock types is commonly interpreted as a result of progressive deformation described in high-grade metagranitoids (Fitz Gerald and Stünitz, 1993; Kruse and Stünitz, 1999; Hasalová et al., 2008a), or alternatively due to an increase in melt fraction (e.g., Toé et al., 2013). Previous studies showed that the deformation gradient in metagranitoids at high temperatures is characterized by the development of augen-gneisses and banded gneisses at higher strains (Handy, 1990; Schulmann and Mlčoch, 1996). Further increase of deformation intensity results in complete disintegration of the layers associated with

resorption of older grains and precipitation of new grains from the percolating fluids and/or melts in the core of the shear zones (Lonka et al., 1998; Hasalová et al., 2008a, 2008b; Oliot et al., 2014). Typical microstructural features of this sequence are the decrease of grain size and progressive disintegration of the compositional layering by crystallization of interstitial unlike phases in host banded aggregates.

The microstructural trend described here is compatible with studied banded orthogneiss, mylonite, and fine-grained granofels sequence (Figs. 8 and 10; Table 1). Therefore, we argue that the granofels represents a zone of highest deformation in heterogeneously deformed metagranitoids, where the banding is disrupted by a combination of melt influx, straining and mechanical mixing (hypothesis 4). In contrast, the hypothesis (1) of a different protolith of studied rock types can be ruled out based on similarity in bulk rock chemistry (Fig. 11) and by similar Cambrian zircon ages (Zulauf et al., 2002; Konopásek et al., 2014) of both granofelses and orthogneisses that suggest similar protolith and origin of these rocks. Similarly, the hypothesis (2) of granodioritic vein intrusions is unlikely due to the lack of euhedral magmatic phenocrysts and related magmatic fabrics, diffuse boundaries with surrounding banded rock types (Fig. 4E), and relatively strong CPO of feldspars that is similar in both the granofels and the orthogneiss (Fig. 9). Hypothesis 3, explaining the granofelses as diatexites with cumulate composition due to melt extraction, cannot be completely ruled out. The latter is compatible with the refractory composition of the granofelses and leucosomes that are depleted in incompatible elements, suggesting their crystallization from residual melts. However, movement of the crystal melt mush en masse is not compatible with the development of CPO, abundant diffuse boundaries with surrounding banded orthogneisses and mylonites, and lack of rotated ghosts or stringers of the host rocks in the granofelses.

There are two possible explanations for the relatively strong CPO fabric intensity in the granofelses: (1) inheritance of deformation fabrics from the orthogneisses that originated during earlier solid-state deformation and were later transformed to granofelses by pervasive grain-scale melt flow, and (2) oriented growth of grains from interstitial melt during granular flow.

The partial inheritance of fabrics is possible, as the fabric patterns of all the phases in both rock types are to some extent similar and granofelses locally contain strings of corroded K-feldspar grains. However, the most likely explanation for the origin of relatively strong fabric of interstitial feldspars in both the mylonite and the granofels is oriented growth of grains by crystallization

from interstitial fluid and/or melt (Menegon et al., 2008; Boneh et al., 2017). This is supported by similarity of CPO fabrics and fabric intensities displayed by interstitial feldspars in host mylonite bands, i.e., plagioclase in K-feldspar and K-feldspar in quartz bands (Figs. 10A, 10B), to those displayed by plagioclase and K-feldspar in the granofels, respectively (Fig. 10C). Another argument for the oriented growth rather than dislocation creep is the lack of subgrains or internal distortion of the small interstitial feldspar grains, which is compatible with their crystallization from interstitial melt (Fig. 12, inset). At the same time, however, CPO fabrics in the mylonitic bands formed dominantly by K-feldspar and quartz (Figs. 10A, 10B), respectively, are compatible with activity of dislocation creep. The CPO pattern in quartz for the mylonite sample EC12-8G can be interpreted in terms of basal <a> slip system. As some of the poles to (0001) occur in the center of the pole figure (Fig. 10B), they suggest a development of a wide single or crossed-girdle c-axis pattern and consequently confirm the correctness of our speculated kinematic section. The dominant slip system in band forming K-feldspar in the mylonite is not clear.

Are Granofelses the Loci of Melt Flow?

We described microstructural features such as narrow films, pools, corroded grain boundaries, and albitic rims (Fig. 9) that indicate the presence of former melt (e.g., Sawyer, 2001; Holness and Sawyer, 2008; Hasalová et al., 2008a). We are aware of the oversimplification of our melt topology quantification approach as the crystallizing melt usually forms overgrowths on preexisting grains and cannot be always identified. The amount of crystallized melt is variable, being highest in migmatites and granofelses (>16 vol%; Table 2) compared to 5–10 vol% in the orthogneisses. However, it has been shown that the amount of crystallized new magmatic phases is not necessarily proportional to the amount of melt that passed through the rock, as the shear zones can be regarded as open systems (Hasalová et al., 2008b, 2008c, 2011; Goncalves et al., 2012). Alternatively, large interstitial oligoclase grains may have crystallized in larger pools, as the composition of minerals crystallized from melt is also related to the available pore space (Holness and Sawyer, 2008). Therefore, the quantified melt contents in this study should be regarded as minimum estimates.

In this context, the identified melt in the granofels may represent only a fraction of the total residual melt, as the fine-grained granoblastic texture reflects crystallization of interstitial melt and resorption of old grains during earlier stages of shear zone history. Our P-T calculations show that at peak conditions (800 °C at 13
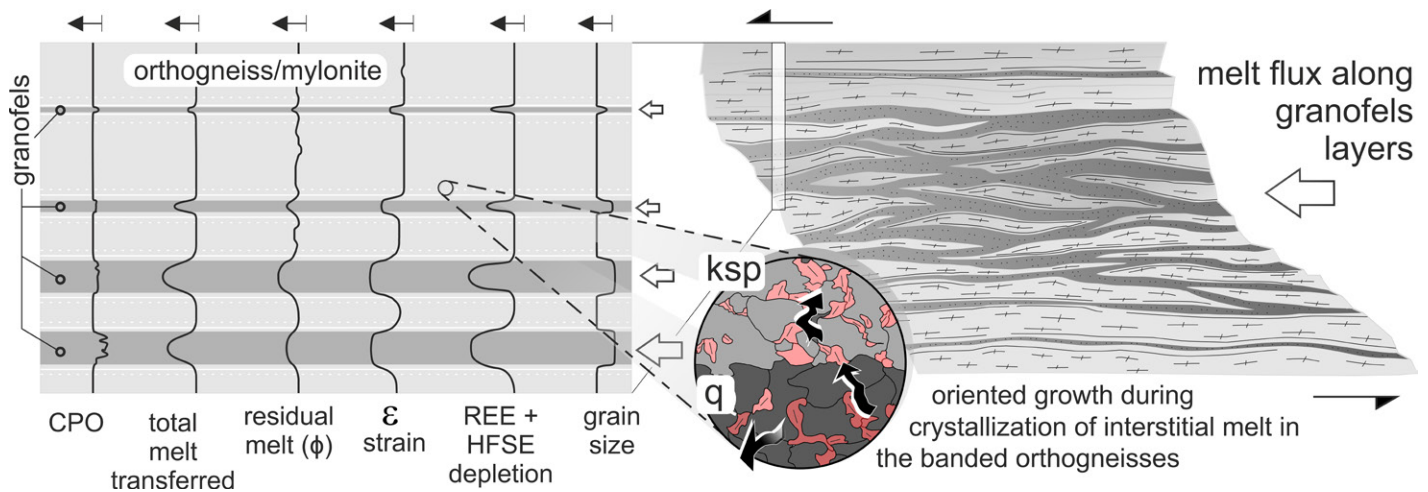
Figure 12. Sketch summarizing the variations of different textural parameters and melt loss-gain relationship as indicated by geochemical signatures across the granofels-orthogneiss contacts. Granofelses represent cores of shear zones, where grain-scale porous melt flow is driven by cavitation pumping or represent the relict traces of porous waves. CPO—crystallographic preferred orientation; REE—rare earth element; HFSE—high field strength element; q—quartz; ksp—potassium feldspar.

kbar) <~6 vol% melt can be produced. Larger melt fraction can be produced only if hydrous fluids were introduced (Weinberg and Hasalová, 2015). We therefore infer that most of the interstitial melt in these rocks originated in external sources and probably migrated from deeper parts of the subducted crust.

If we assume flux of simple granitic melt through the banded orthogneiss, we would expect the granofels to display composition enriched in incompatible elements, specifically the large ion lithophile elements (LILEs), with respect to the surrounding orthogneisses. Instead, comparison of the banded orthogneiss with the granofels shows little differences in major and trace elements. Granofels is slightly depleted in FeO, MgO, TiO$_2$, and Al$_2$O$_3$, reflecting less ferromagnesian minerals like biotite, as well as in incompatible REEs, Cs and Th, and U (HFSEs; Fig. 11). Such a small difference suggests a relatively similar protolith. However, depletion in the incompatible elements can be considered as a result of partial melting of granitic sources, responsible for dissolution of accessory, REE-bearing minerals such as zircon, monazite, xenotime, and apatite in melt and its escape from the system (Janoušek et al., 2004; Lexa et al., 2011). We note that similar chemical changes can result from hydrous fluid percolation (Marquer et al., 1994; Goncalves et al., 2012). However, the described *P-T* conditions of 700–800 °C and >13 kbar do not allow free hydrous fluid percolation and impose stability of silicate melt. Because we cannot constrain total melt transferred in the granofelsic shear zones, or pinpoint precisely the amount of melt that crystallized in respective studied anatectic domains (namely in the granofelses),

it is difficult to speculate on the mode of melt assisted deformation. Melt is usually considered as effectively mobile when its fraction reaches the rheological critical melt percentage (RCMP) of ~25%–30% or similar solid to liquid transition of ~40%–60%, giving rise to diatexites (Arzi, 1978; Rutter and Neumann, 1995; Vigneresse et al., 1996; Vigneresse and Tikoff, 1999; Rosenberg and Handy, 2005). The RCMP could have been easily reached locally and transiently in structurally defined channels represented by S$_1$ layering and S$_2$ fold axial cleavage (Fig. 3D, 3E, 4B, and 4D). Nevertheless, destruction of the deformation layering may occur at lower melt fractions if the deformation mechanism is dominated by grain boundary sliding (granular flow) (Sawyer, 1994, 1996; White et al., 2005). Therefore, complete fabric disintegration and granofels formation can be also explained by continuous reactive porous grain-scale melt flow through dynamic porosity during the granular flow of the grains below the melt connectivity threshold marked by 7–10 vol% (Rosenberg and Handy, 2005). Such transition from banded mylonites to nebulitic migmatites (or granofelses) was convincingly demonstrated by Hasalová et al. (2008a, 2008b, 2008c) for a middle crustal, melt-assisted shear zone. In summary, the granofelses can be interpreted as diatexites that resulted from reactive porous melt flow at grain scale that percolated through highly strained domains in the layered orthogneisses and mylonites (Fig. 12). This scenario assumes that the orthogneisses and mylonites reflect strain gradients in the subducted slab that developed before the partial melting and that such strain gradients were precursory for later pervasive melt flux through the layered sequence.

The melt flow in the high strain zones is accompanied by oriented growth by crystallization of new interstitial phases in host aggregates producing the CPO, higher amount of former melt, depletion of HFSEs and REEs, and high total amount of transferred melt (Fig. 12). Such percolating melt was not in chemical and textural equilibrium with the host rock, and therefore dissolved residual grains and precipitated new interstitial phases (Figs. 9 and 12; Table 2). Such a reactive porous flow is associated with chemical modification of the deformed host rock, as shown in Figure 11.

Mode of Porous Grain-Scale Flow in Granofels

Our microstructural and CPO study (Figs. 8–10) shows that the banded and mylonitic orthogneisses were deformed by dislocation creep combined with melt-assisted grain boundary sliding. In contrast, the granofels underwent melt-enhanced granular flow by unspecified grain-size sensitive deformation mechanisms, and its CPO likely reflects primarily the oriented growth of interstitial grains from melt (Fig. 10). This transition is usually associated with increase of dynamic porosity by dilation of grain boundaries and enhancement of grain-scale fluid and/or melt flow (e.g., Závada et al., 2007; Schulmann et al., 2008b; Fusseis et al., 2009; Okudaira et al., 2015).

The increasing abundance of granofels at the expense of the banded orthogneisses along the studied profile (domains A→C, Fig. 1) can be attributed to porous melt flux from higher melt pressures in deeper levels of the subducting continental slab undergoing partial melting. At high pore pressures, the porous melt flow can

be also driven by larger scale pressure gradients, giving rise to the porous waves or vug waves (Morgan and Holtzman, 2005; Connolly and Podladchikov, 2007), or by compaction-induced segregation (Veveakis et al., 2015; Weinberg et al., 2015). Porous waves are simply described as plume- or lense-shaped batches of melt that migrate through intergranular network of viscoelastic anatectic rocks, where RCMP is transiently reached in the cores of such instabilities.

Geodynamic Consequences of the Localized Porous Melt Flow

We discuss here two contrasting roles of the granofelses during continental subduction: (1) they record the partitioning or localization of deformation in high strain zones that focused porous melt flow and weakening of the crust; and (2) they played a key role in the exhumation

of high-P rocks through development of detachment folds decoupled from continuously subducting continental crust.

Porous Melt Flow and Strain Partitioning During Continental Subduction

The studied sequence of anatectic rocks is interpreted to result from continental subduction of felsic crust of the Saxothuringian lower plate beneath the Teplá-Barrandian upper plate (Konopásek and Schulmann, 2005; Schulmann et al., 2014). These reconstructions are compatible with the P-T conditions estimated for the banded orthogneiss (700°–750° at 9–13 kbar), granofels (780° at 15 kbar), and felsic granulite (750–800 °C at 14–16 kbar; Závada et al., 2007; Konopásek et al., 2014; Kotková et al., 1996) that were subducted into mantle depths and rapidly exhumed. When these data are plotted in the P-T diagram (Fig. 13A) they

outline a typical subduction-type metamorphic gradient with the lowest peak P-T conditions typically developed in the banded orthogneisses and higher P-T conditions in the granofels and granulite. The microstructural evolution from banded orthogneisses to granofels and the prograde P-T trend presented here are consistent with the model of Saxothuringian continental subduction of Chopin et al. (2012); however, in contrast to the latter study, we propose that the granofelses represent zones of active deformation coupled with melt percolation enabling the metamorphic reequilibration. The P-T signature in Figure 13A corresponds to the regional distribution of orthogneiss, granofels, and granulite-rich domains presented in a schematic crustal-scale section (Fig. 13B). The cross section can be subdivided into two regions characterized as domain A and B in the west (increasing proportion of granofels with depth) and domain
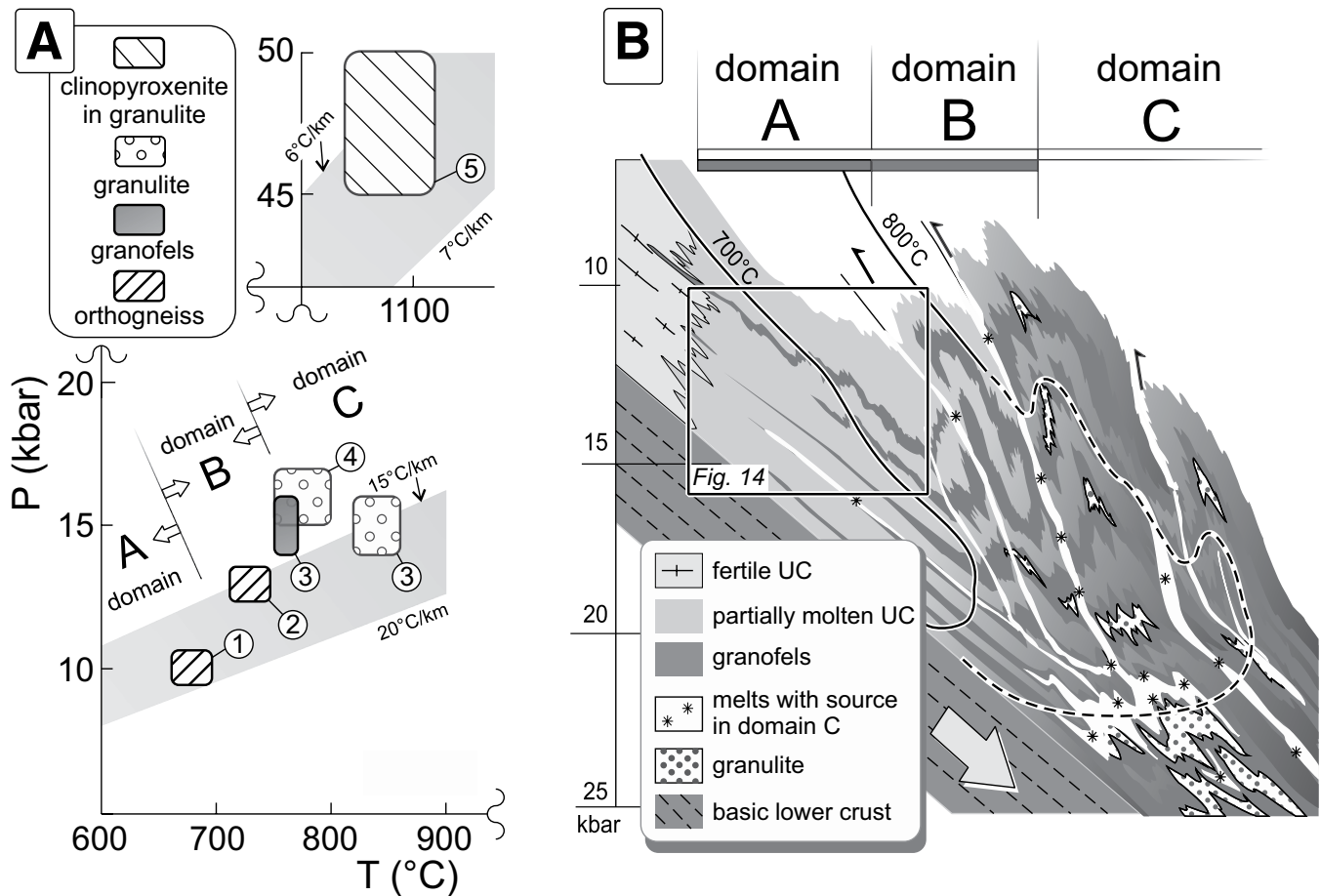
Figure 13. (A) Schematic pressure-temperature (P-T) diagram showing estimated metamorphic conditions for the major lithologies in the Eger Crystalline Complex (ECC) that define a cold geotherm typical of the subduction environment. Numbers in the figures correspond to values presented in: 1—Závada et al. (2007); 2—this study (pseudosection shown in DR File, Fig. DR4); 3—Konopásek et al. (2014); 4—Kotková et al. (1996); 5—Haifler and Kotková (2016). (B) Conceptual sketch of the Variscan continental subduction in Bohemian massif dragging down the continental margin of the lower plate (inspired by Labrousse et al., 2011), showing exhumation by detachment folding and backflow of more deeply subducted portions of the layered sequence juxtaposing ultrahigh-pressure (UHP) granulite-bearing domain C against the high-pressure crust of domain B. UC—upper crust. Black rectangle indicates a detail explaining the nucleation and amplification of detachment folds shown in Figure 14.

C (granofels-granulite region) in the east. We interpret domain C as a source region for the melts percolating upward along zones of localized deformation producing the granofels layers.

This model is fundamentally similar to that explaining Paleozoic eclogitization of subducted Precambrian granulites in the Norwegian Western Gneiss Region (Austrheim, 1987) and the Cenozoic eclogitization of Permian granulites in Italian Alps (Lardeaux and Spalla, 1991). Austrheim (1987) and Lardeaux and Spalla (1991) proposed that the fluids percolated through subducted continental crust along shear zones, leading to progressive eclogitization of deformed and recrystallized anhydrous granulites. The eclogitization is heterogeneous and leads to development of high-P assemblages in localized shear zones surrounding low-strain domains characterized by lower metamorphic grade. In analogy to these studies, we argue that the granofels layers represent Carboniferous high strain zones that equilibrated at higher P-T conditions by percolating melt, compared to the Cambrian–Ordovician orthogneisses, which correspond to low-strain domains, thereby preserving lower P-T conditions.

Exhumation of High-P Rocks through Development of Detachment Folds Decoupled from Subducting Crust

The asymmetrical folding of the layered sequence of anatectic rocks can explain melt percolation triggered exhumation of the low-density felsic crust during continental subduction (Labrousse et al., 2011, 2015). The style of folding and deformation is also similar to that explaining exhumation of eclogites in Scandinavian Caledonides that were exhumed due to progressive weakening of continental crust along eclogite facies (hydrated) shear zones (Jolivet et al., 2005). This style, schematically presented by Labrousse et al. (2011, 2015), is similar to the detachment folds developed above a weak layer (e.g., Blay et al., 1977; Solar and Brown, 2001; Barraud et al., 2004). This folding can be observed on the outcrop scale in domain A (Fig. 4), where the décollement planes probably coincide with boundaries between rheologically weak migmatites or granofelses impregnated by residual interstitial melt and the orthogneisses. This interpretation is supported by melt topology identified in folded granofels layers marked by shape-preferred melt films oriented preferentially

parallel to the axial planar cleavage of asymmetrical folds (Figs. 8B, 8G). Strain incompatibilities during the folding around the arrested tips of deformation zones (Fig. 14) imply stress gradients that redistribute the melts on the grain scale to mesoscale (Kruger and Kisters, 2016). At first, dilatancy can account for thickening of the S_1 parallel leucosomes and influx of weak and melt-containing granofels into the hinge domains of incipient folds (Fig. 7E, 1 in Fig. 14). In the next stage, as the rate of amplification decreases and the system passes to post-buckle flattening (Price and Cosgrove, 1990), the melt pockets and leucosomes align parallel to the axial planar fold cleavage, similar to the melt pockets in the matrix (2 in Fig. 14), in form of compaction-induced melt bands (Figs. 4C, 4D, 8B, and 8G; Weinberg et al., 2015). The melt-coated planes of this planar cleavage are regarded as new transfer zones that can promote retroward transport of the more deeply subducted and folded domains atop the shallower sequences of the same slab (Fig. 13B).

The detachment folding seems to be a key mechanism responsible for exhumation of high-P partially molten sequences along the subduction channel. The exhumation process in the
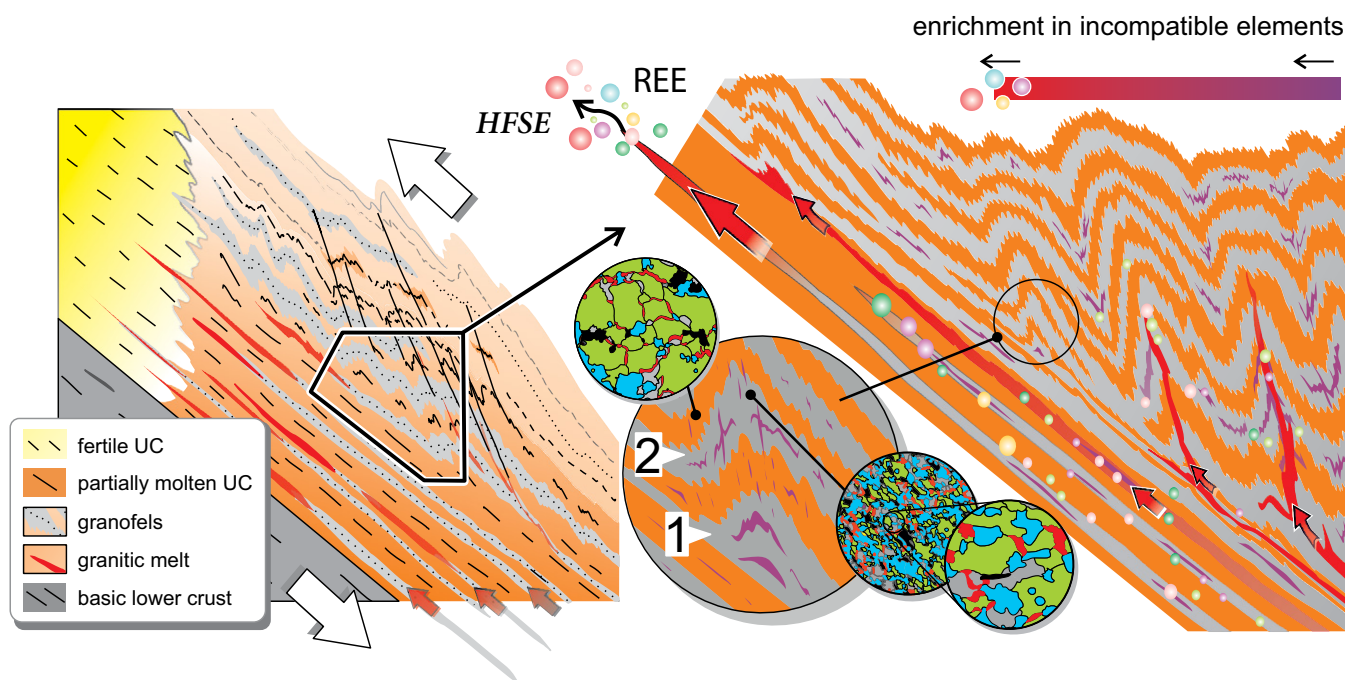
Figure 14. Schematic diagram showing an outcrop-scale detail of the already partially molten crust with upward-directed porous melt flow and detachment folds that form above the migmatitic or granofels layers. UC—upper crust. Direction of porous melt flow and transfer of incompatible elements (rare earth elements, REEs, and high field strength elements, HFSEs) is shown schematically by red arrows. Residual melts (violet color) are redistributed into the hinge zones to form migmatitic patches and isolated fold-axial cleavage parallel leucosomes (Figs. 4C, 4D, 7D, and 7E). Incipient folding at the arrested tips of shear zones (or layer-bound porous waves) at first creates dilatancy that collects residual melt from the granofelses (and orthogneisses) and thickens the S_1 leucosomes (arrow 1 in inset). The second stage of detachment folding is associated with coalescence of melt pockets (arrow 2 in inset) and leucosomes aligned parallel to S_2 fold axial planes. Melt-lubricated fold planes in last stages of the folding represent new zones of weakness that can act as thrusts and accommodate backflow of the more deeply subducted portions of the crust. Gray layers show the granofelses, orange layers are banded orthogneisses, and migrating melt is shown in red.

ECC is probably also driven by buoyancy, as modeled by Labrousse et al. (2015), but likely takes place already at much shallower depths of ~50 km. While the model of Labrousse et al. (2015) shows geometries of exhumed partially molten crustal batches at the scale of several kilometers, the detachment folding can explain backflow of partially molten rocks along the subduction interface at scales ranging from meters to hundreds of meters.

CONCLUSIONS

A model of porous melt flow along the metamorphic layering in high-P felsic crust was established based on detailed field-based structural analysis, microscale melt topology mapping, crystallographic fabric acquisition, thermodynamic equilibria modeling, and whole-rock composition correlations. We have defined zones of porous melt flow that coincide with zones of concentrated deformation and are approximated by the extent of granoblastic granofels layers alternating with migmatized banded orthogneisses and orthogneiss mylonites. Increasing abundance and thickness of these granofels layers are associated with increasing melt pore pressure during granular flow at progressively increasing depths of the subducted slab. Porous melt flow in these deformation zones is reflected by depleted content in incompatible elements in the granofels in contrast to the host-rock orthogneisses, and ubiquitous evidence for grain-scale textures indicative of mineral resorption and precipitation of new grains from interstitial melt. In our model, the granofels layers represent the pathways of throughgoing porous melt flow and are regarded as shear zones that equilibrated at progressively increasing prograde metamorphic conditions of the subduction channel. Moreover, weakening of subducting felsic crust is promoted by redistribution of melt along the shear zones traced by the granofels layers. This weakening facilitated detachment folding at the arrested tips of the shear zones, where melt is driven into the hinge zones and is injected along the axial cleavage of amplifying folds. The detachment folding is regarded as a key mechanism responsible for initiation of exhumation of deeply subducted and partially molten continental crust.

REFERENCES CITED

Arzi, A., 1978, Critical phenomena in the rheology of partially melted rocks: Tectonophysics, v. 44, p. 173–184, https:// doi.org/10.1016/0040-1951(78)90069-0.

Austrheim, H., 1987, Eclogitization of lower crustal granulites by fluid migration through shear zones: Earth and Planetary Science Letters, v. 81, p. 221–232, https://doi.org/10 .1016/0012-821X(87)90158-0.

Bachmann, F., Hielscher, R., and Schaeben, H., 2011, Grain detection from 2D and 3D EBSD data—Specification of the MTEX algorithm: Ultramicroscopy, v. 111, p. 1720–1733, https://doi.org/10.1016/j.ultramic.2011.08.002.

Barraud, J., Gardien, V., Allemand, P., and Grandjean, P., 2004, Analogue models of melt-flow networks in folding migmatites: Journal of Structural Geology, v. 26, p. 307–324, https://doi.org/10.1016/j.jsg.2003.06.002.

Beaumont, C., Jamieson, R., Nguyen, M., and Lee, B., 2001, Himalayan tectonics explained by extrusion of a low-viscosity crustal channel coupled to focused surface denudation: Nature, v. 414, no. 6865, p. 738–742, https://doi .org/10.1038/414738a.

Blay, P., Cosgrove, J., and Summers, J., 1977, An experimental investigation of the development of structures in multilayers under the influence of gravity: Journal of the Geological Society [London], v. 133, p. 329–342, https:// doi.org/10.1144/gsjgs.133.4.0329.

Bonamici, C.E., and Duebendorfer, E.M., 2010, Scale-invariance and self-organized criticality in migmatites of the southern Hualapai Mountains, Arizona: Journal of Structural Geology, v. 32, p. 1114–1124, https://doi.org/10.1016 /j.jsg.2010.06.019.

Boneh, Y., Wallis, D., Hansen, L.N., Krawczynski, M., and Skemer, P., 2017, Oriented grain growth and modification of 'frozen anisotropy' in the lithospheric mantle: Earth and Planetary Science Letters, v. 474, p. 368–374, https://doi .org/10.1016/j.epsl.2017.06.050.

Brown, M., and Solar, G.S., 1999, The mechanism of ascent and emplacement of granite magma during transpression: A syntectonic granite paradigm: Tectonophysics, v. 312, p. 1–33, https://doi.org/10.1016/S0040-1951(99) 00169-9.

Bunge, H., 1982, Texture analysis in materials science: Mathematical models: London, Butterworths, 593 p.

Butler, J.P., Beaumont, C., and Jamieson, R.A., 2015, Paradigm lost: Buoyancy thwarted by the strength of the Western Gneiss Region (ultra) high-pressure terrane, Norway: Lithosphere, v. 7, p. 379–407, https://doi.org/10.1130/L426.1.

Chen, R.X., Ding, B.H., Zheng, Y.F., and Hu, Z.C., 2015, Multiple episodes of anatexis in a collisional orogen: Zircon evidence from migmatite in the Dabie orogen: Lithos, v. 212, p. 247–265, https://doi.org/10.1016/j.lithos.2014.11.004.

Chen, Y.X., Zheng, Y.F., and Hu, Z.C., 2013, Synexhumation anatexis of ultrahigh-pressure metamorphic rocks: Petrological evidence from granitic gneiss in the Sulu orogen: Lithos, v. 156, p. 69–96, https://doi.org/10.1016/j.lithos .2012.10.008.

Chopin, F., Schulmann, K., Štípská, P., Martelat, J.E., Pitra, P., Lexa, O., and Petri, B., 2012, Microstructural and metamorphic evolution of a high-pressure granitic orthogneiss during continental subduction (Orlica-Sniezcnik dome, Bohemian Massif): Journal of Metamorphic Geology, v. 30, p. 347–376, https://doi.org/10.1111/j.1525-1314 .2011.00970.x.

Connolly, J.A.D., and Podladchikov, Y.Y., 2007, Decompaction weakening and channeling instability in ductile porous media: Implications for asthenospheric melt segregation: Journal of Geophysical Research, v. 112, no. B10, B10205, https://doi.org/10.1029/2005JB004213.

Culshaw, N.G., Beaumont, C., and Jamieson, R.A., 2006, The orogenic superstructure-infrastructure concept: Revisited, quantified, and revived: Geology, v. 34, p. 733–736, https://doi.org/10.1130/G22793.1.

Fitz Gerald, J.D., and Stünitz, H., 1993, Deformation of granitoids at low metamorphic grade. 1. Reactions and grain-size reduction: Tectonophysics, v. 221, p. 269–297, https:// doi.org/10.1016/0040-1951(93)90163-E.

Fusseis, F., Regenauer-Lieb, K., Liu, J., Hough, R.M., and De Carlo, F., 2009, Creep cavitation can establish a dynamic granular fluid pump in ductile shear zones: Nature, v. 459, no. 7249, p. 974–977, https://doi.org/10.1038/nature08051.

Ganzhorn, A.C., Labrousse, L., Prouteau, G., Leroy, C., Vrijmoed, J.C., Andersen, T.B., and Arbaret, L., 2014, Structural, petrological and chemical analysis of syn-kinematic migmatites: Insights from the Western Gneiss Region, Norway: Journal of Metamorphic Geology, v. 32, p. 647–673, https://doi.org/10.1111/jmg.12084.

Goncalves, P., Oliot, E., Marquer, D., and Connolly, J.A.D., 2012, Role of chemical processes on shear zone formation: An example from the Grimsel metagranodiorite (Aar massif, Central Alps): Journal of Metamorphic Geology, v. 30, p. 703–722, https://doi.org/10.1111/j.1525-1314 .2012.00991.x.

Gordon, S.M., Whitney, D.L., Teyssier, C., and Fossen, H., 2013, U-Pb dates and trace-element geochemistry of zircon from migmatite, Western Gneiss Region, Norway: Significance for history of partial melting in continental subduction: Lithos, v. 170, p. 35–53, https://doi.org/10.1016 /j.lithos.2013.02.003.

Grant, J.A., 1986, The isocon diagram—A simple solution to Gresens equation for metasomatic alteration: Economic Geology and the Bulletin of the Society of Economic Geologists, v. 81, p. 1976–1982, https://doi.org/10.2113 /gsecongeo.81.8.1976.

Gresens, R., 1967, Composition-volume relationships of metasomatism: Chemical Geology, v. 2, p. 47–65, https://doi .org/10.1016/0009-2541(67)90004-6.

Haifler, J., and Kotková, J., 2016, UHP-UHT peak conditions and near-adiabatic exhumation path of diamond-bearing garnet-clinopyroxene rocks from the Eger Crystalline Complex, North Bohemian Massif: Lithos, v. 248, p. 366–381, https://doi.org/10.1016/j.lithos.2016.02.001.

Hall, D., and Kisters, A., 2012, The stabilization of self-organised leucogranite networks—Implications for melt segregation and far-field melt transfer in the continental crust: Earth and Planetary Science Letters, v. 355, p. 1–12, https://doi.org/10.1016/j.epsl.2012.08.033.

Hall, D., and Kisters, A., 2016, Episodic granite accumulation and extraction from the mid-crust: Journal of Metamorphic Geology, v. 34, p. 483–500, https://doi.org/10.1111 /jmg.12190.

Handy, M.R., 1990, The solid-state flow of polymineralic rocks: Journal of Geophysical Research, v. 95, no. B6, p. 8647–8661, https://doi.org/10.1029/JB095iB06p08647.

Hasalová, P., Schulmann, K., Lexa, O., Štípská, P., Hrouda, F., Ulrich, S., Haloda, J., and Týcova, P., 2008a, Origin of migmatites by deformation-enhanced melt infiltration of orthogneiss: A new model based on quantitative microstructural analysis: Journal of Metamorphic Geology, v. 26, p. 29–53, https://doi.org/10.1111/j.1525-1314 .2007.00743.x.

Hasalová, P., Štípská, P., Powell, R., Schulmann, K., Janoušek, V., and Lexa, O., 2008b, Transforming mylonitic metagranite by open-system interactions during melt flow: Journal of Metamorphic Geology, v. 26, p. 55–80, https:// doi.org/10.1111/j.1525-1314.2007.00744.x.

Hasalová, P., Janoušek, V., Schulmann, K., Štípská, P., and Erban, V., 2008c, From orthogneiss to migmatite: Geochemical assessment of the melt infiltration model in the Gföhl Unit (Moldanubian Zone, Bohemian Massif): Lithos, v. 102, p. 508–537, https://doi.org/10.1016/j.lithos .2007.07.021.

Hasalová, P., Weinberg, R.F., and Macrae, C., 2011, Microstructural evidence for magma confluence and reuse of magma pathways: implications for magma hybridization, Karakoram shear zone in NW India: Journal of Metamorphic Geology, v. 29, p. 875–900, https://doi.org /10.1111/j.1525-1314.2011.00945.x.

Hielscher, R., and Schaeben, H., 2008, A novel pole figure inversion method: Specification of the MTEX algorithm: Journal of Applied Crystallography, v. 41, p. 1024–1037, https://doi.org/10.1107/S0021889808030112.

Hollister, L., 1982, Metamorphic evidence for rapid (2 mm/yr) uplift of a portion of the Central Gneiss Complex, Coast Mountains, BC: Canadian Mineralogist, v. 20, p. 319–332.

Hollister, L., and Crawford, M., 1986, Melt-enhanced deformation: A major tectonic process: Geology, v. 14, p. 558–561, https://doi.org/10.1130/0091-7613(1986)14 <558:MDAMTP>2.0.CO;2.

Holness, M.B., and Sawyer, E.W., 2008, On the pseudomorphing of melt-filled pores during the crystallization of migmatites: Journal of Petrology, v. 49, p. 1343–1363, https://doi.org/10.1093/petrology/egn028.

Holtzman, B.K., Kohlstedt, D.L., Zimmerman, M.E., Heidelbach, F., Hiraga, T., and Hustoft, J., 2003, Melt segregation

and strain partitioning: Implications for seismic anisotropy and mantle flow: Science, v. 301, no. 5637, p. 1227–1230, https://doi.org/10.1126/science.1087132.

Jamieson, R.A., and Beaumont, C., 2011, Coeval thrusting and extension during lower crustal ductile flow—Implications for exhumation of high-grade metamorphic rocks: Journal of Metamorphic Geology, v. 29, p. 33–51, https://doi.org/10.1111/j.1525-1314.2010.00908.x.

Jamieson, R.A., Beaumont, C., Nguyen, M.H., and Culshaw, N.G., 2007, Synconvergent ductile flow in variable-strength continental crust: Numerical models with application to the western Grenville orogen: Tectonics, v. 26, TC5005, https://doi.org/10.1029/2006TC002036.

Jamieson, R.A., Beaumont, C., Warren, C.J., and Nguyen, M.H., 2010, The Grenville Orogen explained? Applications and limitations of integrating numerical models with geological and geophysical data: Canadian Journal of Earth Sciences, v. 47, p. 517–539, https://doi.org/10.1139/E09-070.

Janoušek, V., Finger, F., Roberts, M., Frýda, J., Pin, C., and Dolejš, D., 2004, Deciphering the petrogenesis of deeply buried granites: Whole-rock geochemical constraints on the origin of largely undepleted felsic granulites from the Moldanubian Zone of the Bohemian Massif: Royal Society of Edinburgh Transactions, Earth Sciences, v. 95, p. 141–159, https://doi.org/10.1017/S0263593300000985.

Jolivet, L., Raimbourg, H., Labrousse, L., Avigad, D., Leroy, Y., Austrheim, H., and Andersen, T.B., 2005, Softening triggerred by eclogitization, the first step toward exhumation during continental subduction: Earth and Planetary Science Letters, v. 237, p. 532–547, https://doi.org/10.1016/j.epsl.2005.06.047.

Kisters, A.F.M., Ward, R.A., Anthonissen, C.J., and Vietze, M.E., 2009, Melt segregation and far-field melt transfer in the mid-crust: Journal of the Geological Society [London], v. 166, p. 905–918, https://doi.org/10.1144/0016-76492009-012.

Kohlstedt, D., and Holtzman, B., 2009, Shearing melt out of the earth: An experimentalist's perspective on the influence of deformation on melt extraction: Annual Review of Earth and Planetary Sciences, v. 37, p. 561–593, https://doi.org/10.1146/annurev.earth.031208.100104.

Konopásek, J., and Schulmann, K., 2005, Contrasting Early Carboniferous field geotherms: Evidence for accretion of a thickened orogenic root and subducted Saxothuringian crust (Central European Variscides): Journal of the Geological Society [London], v. 162, p. 463–470, https://doi.org/10.1144/0016-764904-004.

Konopásek, J., Pilátová, E., Košler, J., and Sláma, J., 2014, Zircon (re)crystallization during short-lived, high-P granulite facies metamorphism (Eger Complex, NW Bohemian Massif): Journal of Metamorphic Geology, v. 32, p. 885–902, https://doi.org/10.1111/jmg.12098.

Korchinski, M.S., Vry, J., Little, T.A., Millet, M.A., Bicknell, R., Smith, E., and von der Handt, A., 2014, Timing of UHP exhumation and rock fabric development in gneiss domes containing the world's youngest eclogite facies rocks, southeastern Papua New Guinea: Journal of Metamorphic Geology, v. 32, p. 1019–1039, https://doi.org/10.1111/jmg.12105.

Košler, J., Bowes, D.R., Konopasek, J., and Míkova, J., 2004, Laser ablation ICPMS dating of zircons in Erzgebirge orthogneisses: Evidence for early Cambrian and Early Ordovician granitic plutonism in the western Bohemian Massif: European Journal of Mineralogy, v. 16, p. 15–22, https://doi.org/10.1127/0935-1221/2004/0016-0015.

Kotková, J., and Janák, M., 2015, UHP kyanite eclogite associated with garnet peridotite and diamond-bearing granulite, northern Bohemian Massif: Lithos, v. 226, p. 255–264, https://doi.org/10.1016/j.lithos.2015.01.016.

Kotková, J., Kröner, A., Todt, W., and Fiala, J., 1996, Zircon dating of north Bohemian granulites, Czech Republic: Further evidence for the lower carboniferous high-pressure event in the Bohemian Massif: Geologische Rundschau, v. 85, p. 154–161, https://doi.org/10.1007/s005310050064.

Kotková, J., O'Brien, P.J., and Ziemann, M.A., 2011, Diamond and coesite discovered in Saxony-type granulite: Solution to the Variscan garnet peridotite enigma: Geology, v. 39, p. 667–670, https://doi.org/10.1130/G31971.1.

Kruger, T., and Kisters, A., 2016, Magma accumulation and segregation during regional-scale folding: The Holland's dome granite injection complex, Damara belt, Namibia: Journal of Structural Geology, v. 89, p. 1–18, https://doi.org/10.1016/j.jsg.2016.05.002.

Kruse, R., and Stünitz, H., 1999, Deformation mechanisms and phase distribution in mafic high-temperature mylonites from the Jotun Nappe, southern Norway: Tectonophysics, v. 303, p. 223–249, https://doi.org/10.1016/S0040-1951(98)00255-8.

Labrousse, L., Prouteau, G., and Ganzhorn, A.C., 2011, Continental exhumation triggered by partial melting at ultrahigh pressure: Geology, v. 39, p. 1171–1174, https://doi.org/10.1130/G32316.1.

Labrousse, L., Duretz, T., and Gerya, T., 2015, H₂O-fluid-saturated melting of subducted continental crust facilitates exhumation of ultrahigh-pressure rocks in continental subduction zones: Earth and Planetary Science Letters, v. 428, p. 151–161, https://doi.org/10.1016/j.epsl.2015.06.016.

Lardeaux, J.M., and Spalla, M.I., 1991, From granulites to eclogites in the Sesia Zone (Italian Western Alps)—A record of the opening and closure of the Piedmont Ocean: Journal of Metamorphic Geology, v. 9, p. 35–59, https://doi.org/10.1111/j.1525-1314.1991.tb00503.x.

Lexa, O., Štípská, P., Schulmann, K., Baratoux, L., and Kröner, A., 2005, Contrasting textural record of two distinct metamorphic events of similar P-T conditions and different durations: Journal of Metamorphic Geology, v. 23, p. 649–666, https://doi.org/10.1111/j.1525-1314.2005.00601.x.

Lexa, O., Schulmann, K., Janoušek, V., Štípská, P., Guy, A., and Racek, M., 2011, Heat sources and trigger mechanisms of exhumation of HP granulites in Variscan orogenic root: Journal of Metamorphic Geology, v. 29, p. 79–102, https://doi.org/10.1111/j.1525-1314.2010.00906.x.

Lonka, H., Schulmann, K., and Venera, Z., 1998, Ductile deformation of tonalite in the Suomusjarvi shear zone, south-western Finland: Journal of Structural Geology, v. 20, p. 783–798, https://doi.org/10.1016/S0191-8141(98)00003-0.

López-Moro, F.J., 2012, EASYGRESGRANT—A Microsoft Excel spreadsheet to quantify volume changes and to perform mass-balance modeling in metasomatic systems: Computers & Geosciences, v. 39, p. 191–196, https://doi.org/10.1016/j.cageo.2011.07.014.

Maierová, P., Čadek, O., Lexa, O., and Schulmann, K., 2012, A numerical model of exhumation of the orogenic lower crust in the Bohemian Massif during the Variscan orogeny: Studia Geophysica et Geodaetica, v. 56, p. 595–619, https://doi.org/10.1007/s11200-011-0455-x.

Maierová, P., Schulmann, K., Lexa, O., Guillot, S., Štípská, P., Janoušek, V.V., and Čadek, O., 2016, European Variscan orogenic evolution as an analogue of Tibetan-Himalayan orogen: Insights from petrology and numerical modeling: Tectonics, v. 35, p. 1760–1780, https://doi.org/10.1002/2015TC004098.

Marquer, D., Petrucci, E., and Iacumin, P., 1994, Fluid advection in shear zones—Evidence from geological and geochemical relationships in the Aiguilles-rouges Massif (western Alps, Switzerland): Schweizerische Mineralogische und Petrographische Mitteilungen, v. 74, p. 137–148.

McKenzie, D., 1984, The generation and compaction of partially molten rock: Journal of Petrology, v. 25, p. 713–765, https://doi.org/10.1093/petrology/25.3.713.

Menegon, L., Pennacchioni, G., and Spiess, R., 2008, Dissolution-precipitation creep of K-feldspar in mid-crustal granite mylonites: Journal of Structural Geology, v. 30, p. 565–579, https://doi.org/10.1016/j.jsg.2008.02.001.

Mlčoch, B., and Konopásek, J., 2010, Pre-Late Carboniferous geology along the contact of the Saxothuringian and Teplá-Barrandian zones in the area covered by younger sediments and volcanics (western Bohemian Massif, Czech Republic): Journal of Geosciences, v. 55, p. 81–94, https://doi.org/10.3190/jgeosci.068.

Möller, C., Andersson, J., Dyck, B., and Lundin, I.A., 2015, Exhumation of an eclogite terrane as a hot migmatitic nappe, Sveconorwegian orogen: Lithos, v. 226, p. 147–168, https://doi.org/10.1016/j.lithos.2014.12.013.

Morgan, J.P., and Holtzman, B.K., 2005, Vug waves: A mechanism for coupled rock deformation and fluid migration: Geochemistry, Geophysics, Geosystems, v. 6, Q08002, https://doi.org/10.1029/2004GC000818.

Nasdala, L., and Massonne, H.J., 2000, Microdiamonds from the Saxonian Erzgebirge, Germany: In situ micro-Raman characterisation: European Journal of Mineralogy, v. 12, p. 495–498, https://doi.org/10.1127/0935-1221/2000/0012-0495.

Okudaira, T., Jeřábek, P., Stünitz, H., and Fusseis, F., 2015, High-temperature fracturing and subsequent grain-size-sensitive creep in lower crustal gabbros: Evidence for co-seismic loading followed by creep during decaying stress in the lower crust?: Journal of Geophysical Research, v. 120, p. 3119–3141, https://doi.org/10.1002/2014JB011708.

Oliot, E., Goncalves, P., Schulmann, K., Marquer, D., and Lexa, O., 2014, Mid-crustal shear zone formation in granitic rocks: Constraints from quantitative textural and crystallographic preferred orientations analyses: Tectonophysics, v. 612, p. 63–80, https://doi.org/10.1016/j.tecto.2013.11.032.

Peč, M., Holtzman, B.K., Zimmerman, M., and Kohlstedt, D.L., 2015, Reaction infiltration instabilities in experiments on partially molten mantle rocks: Geology, v. 43, p. 575–578, https://doi.org/10.1130/G36611.1.

Potdevin, J.L., and Marquer, D., 1987, Quantitative methods for the estimation of mass transfers by fluids in deformed metamorphic rocks (Méthodes de quantification des transferts de matière par les fluides dans les roches métamorphiques déformées): Geodinamica Acta, v. 1, p. 193–206, https://doi.org/10.1080/09853111.1987.11105138.

Price, N., and Cosgrove, J.W., 1990, Analysis of geological structures: Cambridge, UK, Cambridge University Press, 502 p.

Ramsay, J.G., and Huber, M.I., 1987, The Techniques of Modern Structural Geology, Volume 2: Folds and Fractures: London, Academic Press, 391 p.

Rosenberg, C.L., and Handy, M.R., 2000, Syntectonic melt pathways during simple shearing of a partially molten rock analogue (Norcamphor-Benzamide): Journal of Geophysical Research, v. 105, no. B2, p. 3135–3149, https://doi.org/10.1029/1999JB900371.

Rosenberg, C.L., and Handy, M.R., 2005, Experimental deformation of partially melted granite revisited: Implications for the continental crust: Journal of Metamorphic Geology, v. 23, p. 19–28, https://doi.org/10.1111/j.1525-1314.2005.00555.x.

Rutter, E.H., and Neumann, D.H.K., 1995, Experimental deformation of partially molten westerly granite under fluid-absent conditions, with implications for the extraction of granitic magmas: Journal of Geophysical Research, v. 100, no. B8, p. 15,697–15,715, https://doi.org/10.1029/94JB03388.

Sawyer, E.W., 1994, Melt segregation in the continental crust: Geology, v. 22, p. 1019–1022, https://doi.org/10.1130/0091-7613(1994)022.

Sawyer, E.W., 1996, Melt segregation and magma flow in migmatites: Implications for the generation of granite magmas: Royal Society of Edinburgh Transactions, Earth Sciences, v. 87, p. 85–94, https://doi.org/10.1017/S0263593300006507.

Sawyer, E.W., 2001, Melt segregation in the continental crust: Distribution and movement of melt in anatectic rocks: Journal of Metamorphic Geology, v. 19, p. 291–309, https://doi.org/10.1046/j.0263-4929.2000.00312.x.

Sawyer, E.W., 2008, Atlas of migmatites: Canadian Mineralogist Special Publication 9, 371 p.

Sawyer, E.W., 2014, The inception and growth of leucosomes: microstructure at the start of melt segregation in migmatites: Journal of Metamorphic Geology, v. 32, p. 695–712, https://doi.org/10.1111/jmg.12088.

Schulmann, K., Lexa, O., Štípská, P., Racek, M., Tajcmanová, L., Konopásek, J., Edel, J.B., Peschler, A., and Lehmann, J., 2008a, Vertical extrusion and horizontal channel flow of orogenic lower crust: Key exhumation mechanisms in large hot orogens?: Journal of Metamorphic Geology, v. 26, p. 273–297, https://doi.org/10.1111/j.1525-1314.2007.00755.x.

Schulmann, K., Martelat, J.E., Ulrich, S., Lexa, O., Štípská, P., and Becker, J.K., 2008b, Evolution of microstructure and melt topology in partially molten granitic mylonite: Implications for rheology of felsic middle crust: Journal of Geophysical Research, v. 113, no. B10, B10406, https://doi.org/10.1029/2007JB005508.

Schulmann, K., Konopásek, J., Janoušek, V., Lexa, O., Lardeaux, J.M., Edel, J.B., Štípská, P., and Ulrich, S., 2009, An Andean type Palaeozoic convergence in the Bohemian Massif: Comptes Rendus Geoscience, v. 341, p. 266–286, https://doi.org/10.1016/j.crte.2008.12.006.

Schulmann, K., Lexa, O., Janoušek, V., Lardeaux, J.M., and Edel, J.B., 2014, Anatomy of a diffuse cryptic suture zone: An example from the Bohemian Massif, European Variscides: Geology, v. 42, p. 275–278, https://doi.org/10.1130/G35290.1.

Solar, G.S., and Brown, M., 2001, Deformation partitioning during transpression in response to Early Devonian oblique convergence, northern Appalachian orogen, USA: Journal of Structural Geology, v. 23, p. 1043–1065, https://doi.org/10.1016/S0191-8141(00)00175-9.

Stepanov, A.S., Hermann, J., Rubatto, D., Korsakov, A.V., and Danyushevsky, L.V., 2016, Melting history of an ultrahigh-pressure paragneiss revealed by multiphase solid inclusions in garnet, Kokchetav Massif, Kazakhstan: Journal of Petrology, v. 57, p. 1531–1554, https://doi.org/10.1093/petrology/egw049.

Stöckhert, B., Duyster, J., Trepmann, C., and Massonne, H.J., 2001, Microdiamond daughter crystals precipitated from supercritical COH plus silicate fluids included in garnet, Erzgebirge, Germany: Geology, v. 29, p. 391–394, https://doi.org/10.1130/0091-7613(2001)029<0391:MDCPFS>2.0.CO;2.

Tichomirowa, M., Berger, H.J., Koch, E.A., Belyatski, B.V., Gotze, J., Kempe, U., Nasdala, L., and Schaltegger, U., 2001, Zircon ages of high-grade gneisses in the Eastern Erzgebirge (Central European Variscides)—Constraints on origin of the rocks and Precambrian to Ordovician magmatic events in the Variscan foldbelt: Lithos, v. 56, p. 303–332, https://doi.org/10.1016/S0024-4937(00)00066-9.

Toé, W., Vanderhaeghe, O., Andre-Mayer, A.S., Feybesse, J.L., and Milesi, J.P., 2013, From migmatites to granites in the Pan-African Damara orogenic belt, Namibia: Journal of African Earth Sciences, v. 85, p. 62–74, https://doi.org/10.1016/j.jafrearsci.2013.04.009.

Vanderhaeghe, O., 1999, Pervasive melt migration from migmatites to leucogranite in the Shuswap metamorphic core complex, Canada: Control of regional deformation: Tectonophysics, v. 312, p. 35–55, https://doi.org/10.1016/S0040-1951(99)00171-7.

Vanderhaeghe, O., 2001, Melt segregation, pervasive melt migration and magma mobility in the continental crust: The structural record from pores to orogens: Physics and Chemistry of the Earth, v. 26, p. 213–223, https://doi.org/10.1016/S1464-1895(01)00048-5.

Vanderhaeghe, O., 2009, Migmatites, granites and orogeny: Flow modes of partially-molten rocks and magmas associated with melt/solid segregation in orogenic belts: Tectonophysics, v. 477, p. 119–134, https://doi.org/10.1016/j.tecto.2009.06.021.

Vanderhaeghe, O., Medvedev, S., Fullsack, P., Beaumont, C., and Jamieson, R.A., 2003, Evolution of orogenic wedges and continental plateaux: Insights from crustal thermal-mechanical models overlying subducting mantle lithosphere: Geophysical Journal International, v. 153, p. 27–51, https://doi.org/10.1046/j.1365-246X.2003.01861.x.

Vernon, R.H., and Paterson, S.R., 2001, Axial-surface leucosomes in anatectic migmatites: Tectonophysics, v. 335, p. 183–192, https://doi.org/10.1016/S0040-1951(01)00049-X.

Veveakis, E., Regenauer-Lieb, K., and Weinberg, R.F., 2015, Ductile compaction of partially molten rocks: The effect of non-linear viscous rheology on instability and segregation: Geophysical Journal International, v. 200, p. 519–523, https://doi.org/10.1093/gji/ggu412.

Vigneresse, J.L., and Tikoff, B., 1999, Strain partitioning during partial melting and crystallizing felsic magmas: Tectonophysics, v. 312, p. 117–132, https://doi.org/10.1016/S0040-1951(99)00167-5.

Vigneresse, J.L., Barbey, P., and Cuney, M., 1996, Rheological transitions during partial melting and crystallization with application to felsic magma segregation and transfer: Journal of Petrology, v. 37, p. 1579–1600, https://doi.org/10.1093/petrology/37.6.1579.

Wallner, H., and Schmeling, H., 2016, Numerical models of mantle lithosphere weakening, erosion and delamination induced by melt extraction and emplacement: International Journal of Earth Sciences, v. 105, p. 1741–1760, https://doi.org/10.1007/s00531-016-1343-y.

Weinberg, R.F., and Hasalová, P., 2015, Water-fluxed melting of the continental crust: A review: Lithos, v. 212, p. 158–188, https://doi.org/10.1016/j.lithos.2014.08.021.

Weinberg, R.F., and Regenauer-Lieb, K., 2010, Ductile fractures and magma migration from source: Geology, v. 38, p. 363–366, https://doi.org/10.1130/G30482.1.

Weinberg, R.F., Veveakis, E., and Regenauer-Lieb, K., 2015, Compaction-driven melt segregation in migmatites: Geology, v. 43, p. 471–474, https://doi.org/10.1130/G36562.1.

White, J.C., and White, S.H., 1981, On the structure of grain boundaries in tectonites: Tectonophysics, v. 78, p. 613–628, https://doi.org/10.1016/0040-1951(81)90032-9.

White, R.W., Pomroy, N.E., and Powell, R., 2005, An in situ metatexite-diatexite transition in upper amphibolite facies rocks from Broken Hill, Australia: Journal of Metamorphic Geology, v. 23, p. 579–602, https://doi.org/10.1111/j.1525-1314.2005.00597.x.

Yarushina, V.M., Podladchikov, Y.Y., and Connolly, J.A.D., 2015, (De)compaction of porous viscoelastoplastic media: Solitary porosity waves: Journal of Geophysical Research, v. 120, p. 4843–4862, https://doi.org/10.1002/2014JB011260.

Závada, P., Schulmann, K., Konopásek, J., Ulrich, S., and Lexa, O., 2007, Extreme ductility of feldspar aggregates—Melt-enhanced grain boundary sliding and creep failure: Rheological implications for felsic lower crust: Journal of Geophysical Research, v. 112, no. B10, B10210, https://doi.org/10.1029/2006JB004820.

Zhang, L., Chen, R.X., Zheng, Y.F., and Hu, Z., 2015, Partial melting of deeply subducted continental crust during exhumation: insights from felsic veins and host UHP metamorphic rocks in North Qaidam, northern Tibet: Journal of Metamorphic Geology, v. 33, p. 671–694, https://doi.org/10.1111/jmg.12146.

Zulauf, G., Dörr, W., Fiala, J., Kotková, J., Maluski, H., and Valverde-Vaquero, P., 2002, Evidence for high-temperature diffusional creep preserved by rapid cooling of lower crust (North Bohemian shear zone, Czech Republic): Terra Nova, v. 14, p. 343–354, https://doi.org/10.1046/j.1365-3121.2002.00424.x.